THE EUROPEAN
PHYSICAL JOURNAL A

Hyperon–nucleon interaction in chiral effective field theory at next-to-next-to-leading order

Johann Haidenbauer[1,a] , **Ulf-G. Meißner**[3,1,2,4,b] , **Andreas Nogga**[1,2,c] , **Hoai Le**[1,d]

[1] IAS-4, IKP-3 and JHCP, Forschungszentrum Jülich, 52428 Jülich, Germany
[2] CASA, Forschungszentrum Jülich, 52425 Jülich, Germany
[3] HISKP and BCTP, Universität Bonn, 53115 Bonn, Germany
[4] Tbilisi State University, 0186 Tbilisi, Georgia

Abstract A hyperon–nucleon potential for the strangeness $S = -1$ sector (ΛN, ΣN) up to third order in the chiral expansion is presented. SU(3) flavor symmetry is imposed for constructing the interaction, however, the explicit SU(3) symmetry breaking by the physical masses of the pseudoscalar mesons and in the leading-order contact terms is taken into account. A novel regularization scheme is employed which has already been successfully used in studies of the nucleon–nucleon interaction within chiral effective field theory up to high orders. An excellent description of the low-energy Λp, $\Sigma^- p$ and $\Sigma^+ p$ scattering data is achieved. New data from J-PARC on angular distributions for the ΣN channels are analyzed. Results for the hypertriton and $A = 4$ hyper-nuclear separation energies are presented. An uncertainty estimate for the chiral expansion is performed for selected hyperon–nucleon observables.

1 Introduction

The hyperon–nucleon (ΛN, ΣN) interaction has been under scrutiny in various fields in recent times. Certainly most prominent has been the discussion of its properties in an astrophysical context. The discovery of neutron stars with masses around or in excess of twice the solar mass opened speculations about the role hyperons and specifically the Λ play in understanding their characteristics. In particular, at densities realized in such compact objects, neutrons should be eventually converted to Λ's, resulting in a softening of the equation-of-state (EoS) and a collapse of the conventional theoretical explanation of the observed mass-radius relation. This is the so-called hyperon puzzle, cf. the reviews [1–5] and references therein. On a less spectacular (speculative) level, new measurements of ΛN and ΣN scattering have been reported [6–9], including the first more extensive data on $\Sigma^+ p$ and $\Sigma^- p$ differential cross sections away from the threshold. In addition, two-particle momentum correlation functions involving strange baryons have been determined, in heavy-ion collision and in high-energy pp collisions, which allow access to the YN interaction at very low momenta [10–13]. Finally, there are ongoing efforts for a better determination of the binding energies of light Λ hypernuclei [14–16]. On the theory side, lattice QCD simulations have matured to a stage where an evaluation of the YN interaction for quark (pion) masses close to the physical point can be performed [17,18]. Further, *ab initio* methods like the no-core shell model (NCSM) have been pushed to a level where calculations of hypernuclei up to $A = 10$ and beyond can be performed, incorporating the full complexity of the underlying elementary YN interaction [19–25].

Chiral effective field theory (EFT) for nuclear systems, formulated by Weinberg about 30 years ago [26,27], constitutes a rather powerful tool for studying the interaction between baryons. In this approach a potential is established via an expansion in terms of small momenta and the pion mass, subject to an appropriate power counting, so that the results can be improved systematically by going to higher orders, while at the same time theoretical uncertainties can be estimated [28,29]. Furthermore, two- and three-baryon forces can be constructed in a consistent way. The resulting interaction potentials can be readily employed in standard two- and few-body calculations. They consist of contributions from an increasing number of pseudoscalar-meson

[a] e-mail: j.haidenbauer@fz-juelich.de

[b] e-mail: meissner@hiskp.uni-bonn.de (corresponding author)

[c] e-mail: a.nogga@fz-juelich.de

[d] e-mail: h.le@fz-juelich.de

exchanges, determined by the underlying chiral symmetry, and of contact terms which encode the unresolved short-distance dynamics and whose strengths are parameterized by a priori unknown low-energy constants (LECs). Of course, there are further LECs related to higher order two-meson exchanges which can in principle be fixed from meson-baryon scattering data.

While the description of the nucleon–nucleon (NN) interaction within chiral EFT has already progressed up to the fifth order and beyond [30–32], corresponding applications of that framework to the YN interaction are lagging far behind [33–37]. Here, NLO is presently the state-of-the-art [38–41]. That status is primarily a consequence of the unsatisfactory situation with regard to the data base, practically only cross sections are available and primarily for energies near the thresholds. In particular, differential observables that would allow to fix the LECs in P- and/or higher partial waves, which emerge in the chiral expansion when going to higher orders, are rather scarce and of low statistics. Only within the last few years the overall circumstances became more promising, thanks to the E40 experiment performed at the J-PARC facility. The measurements have already produced differential cross sections for the $\Sigma^+ p$ and $\Sigma^- p$ channels for laboratory momenta from 440 to 850 MeV/c [7–9] and corresponding studies for Λp, including possibly even spin-dependent observables, are in the stage of preparation [42].

In this paper, we present a YN potential up to next-to-next-to-leading order (N²LO), derived within SU(3) chiral EFT. The mentioned experimental development was one of the motivations to extend our study of the ΛN-ΣN interaction to the next order. However, there are also several theoretical aspects which make an extension to N²LO rather interesting. One of them is that in the Weinberg counting three-baryon forces (3BFs) emerge at this order. Calculations of the four-body systems ${}^4_\Lambda$H and ${}^4_\Lambda$He for the NLO13 [38] and NLO19 [39] potentials based on Faddeev-Yakubovsky equations indicate that the experimental separation energies are underestimated and dependent on the version of the YN interaction [39]. Very likely this signals the need for including ΛNN and possibly also ΣNN 3BFs [43]. Another appealing factor is (in view of the mentioned scarcity of data) that no additional LECs appear at this order. At the same time, results for NN scattering indicate that there is some improvement in the energy dependence of the S-waves and, specifically, in several P-waves once the contributions involving the sub-leading πN vertices that enter at N²LO are taken into account.

A further issue is the dependence on the regulator that has to be introduced to remove high-momentum components when solving the scattering equations [44]. In general, a substantial reduction of the residual regulator dependence can be achieved by going to high orders with a larger number of LECs, which then allow one to absorb those effects efficiently [45]. Since our calculation is only up to N²LO, we want to keep regulator artifacts as small as possible from the beginning. With regard to that, a novel regularization scheme proposed and applied in Ref. [31] seems to be rather promising. Here, a local regulator is applied to the pion-exchange contributions and only the contact terms, being non-local by themselves, are regularized with a non-local function. Accordingly, the resulting interactions are called "semilocal momentum-space regularized (SMS) chiral NN potentials" [31]. In earlier works on the NN interaction but also in our YN studies, a non-local cutoff has been applied to the whole potential [38,39,44]. A local regulator for pion-exchange contributions leads to a reduction of the distortion in the long-range part of the interaction and, thereby, facilitates a more rapid convergence already at low chiral orders. Of course, this effect cannot be directly quantified in case of ΛN and ΣN because of the lack of more detailed empirical information, specifically due to the absence of a proper partial-wave analysis. Nonetheless, given that we aim at comparing our results with the new J-PARC data at laboratory momenta around 500 MeV/c, a reduction of regulator artifacts is definitely desirable.

The paper is structured in the following way: In Sect. 2, we summarize the basics of the employed formalism. More details are described in an appendix. Our results are presented in Sect. 3 where we discuss in detail the scattering cross sections for the channels Λp, $\Sigma^+ p$ and $\Sigma^- p$. Predictions for S- and P-wave phase shifts in the ΛN and ΣN (isospin $I = 3/2$) channels are also provided. Furthermore, results for the hypertriton and $A = 4$ hyper-nuclear separation energies and for the in-medium properties of the Λ and Σ hyperons are given. Finally, an uncertainty estimate of our EFT calculations is presented. The paper closes with a brief summary and an outlook.

2 Formalism

In this section and in Appendix A, we provide a self-contained description of all the ingredients of the new YN interaction and its extension to N²LO. However, we refrain from repeating here the details of the derivation of the baryon-baryon interaction within SU(3) chiral EFT. This has been described and thoroughly discussed in Refs. [34,38] and in the review [46]. We refer the interested reader to those works. Also, with regard to various aspects of the new regularization scheme that forms the basis of the SMS potentials, we refer to Ref. [31] for details where this procedure was introduced and worked out.

2.1 One-boson exchange

Let us start with the one-boson-exchange (OBE) contribution and with introducing the new regularization scheme. The formulae for the contributions from two-boson exchanges which arise at NLO and N²LO are given in Appendix A. The regularized potential for single-meson exchange V_P ($P = \pi, K, \eta$) has the following form in momentum space:

$$
V^{\mathrm{OBE}}_{B_1 B_2 \to B_3 B_4}(\mathbf{q})
$$
$$
= -f_{B_1 B_3 P} f_{B_2 B_4 P} \left(\frac{\boldsymbol{\sigma_1} \cdot \mathbf{q}\, \boldsymbol{\sigma_2} \cdot \mathbf{q}}{\mathbf{q}^2 + M_P^2} + C(M_P)\, \boldsymbol{\sigma_1} \cdot \boldsymbol{\sigma_2} \right)
$$
$$
\times \exp\left(-\frac{\mathbf{q}^2 + M_P^2}{\Lambda^2} \right) \mathcal{I}_{B_1 B_2 \to B_3 B_4}, \qquad (1)
$$

where the $f_{B_i B_j P}$ are baryon-baryon-meson coupling constants, M_P is the mass of the exchanged pseudoscalar meson, and $\mathcal{I}_{B_1 B_2 \to B_3 B_4}$ is the pertinent isospin factor. The transferred momentum $\mathbf{q}$ is defined in terms of the final and initial center-of-mass (c.m.) momenta of the baryons, $\mathbf{p}'$ and $\mathbf{p}$, as $\mathbf{q} = \mathbf{p}' - \mathbf{p}$. We adopt here the convention of Ref. [31] to include a leading-order contact term in the one-boson exchange potential. It is chosen in such a way that the (total) spin-spin part of the potential vanishes for $r \to 0$ in the configuration-space representation. The expression of $C(M_P)$ which fulfills that requirement can be given in analytical form and amounts to [31]

$$
C(M_P) = -\left[\Lambda \left(\Lambda^2 - 2M_P^2 \right) \right.
$$
$$
\left. + 2\sqrt{\pi} M_P^3 \exp\left(\frac{M_P^2}{\Lambda^2} \right) \mathrm{erfc}\left(\frac{M_P}{\Lambda} \right) \right] / (3\Lambda^3).
$$
$$
(2)
$$

Here, $\mathrm{erfc}(x)$ is the complementary error function

$$
\mathrm{erfc}(x) = \frac{2}{\sqrt{\pi}} \int_x^\infty dt\, e^{-t^2}. \qquad (3)
$$

Under the assumption of strict SU(3) flavor symmetry, the various coupling constants $f_{B_i B_j P}$ are related to each other by [47]

$$
\begin{aligned}
f_{NN\pi} &= f, & f_{NN\eta_8} &= \tfrac{1}{\sqrt{3}}(4\alpha - 1)f, \\
f_{\Lambda NK} &= -\tfrac{1}{\sqrt{3}}(1 + 2\alpha)f, & f_{\Xi\Xi\pi} &= -(1 - 2\alpha)f, \\
f_{\Xi\Xi\eta_8} &= -\tfrac{1}{\sqrt{3}}(1 + 2\alpha)f, & f_{\Xi\Lambda K} &= \tfrac{1}{\sqrt{3}}(4\alpha - 1)f, \\
f_{\Lambda\Sigma\pi} &= \tfrac{2}{\sqrt{3}}(1 - \alpha)f, & f_{\Sigma\Sigma\eta_8} &= \tfrac{2}{\sqrt{3}}(1 - \alpha)f, \\
f_{\Sigma NK} &= (1 - 2\alpha)f, & f_{\Sigma\Sigma\pi} &= 2\alpha f, \\
f_{\Lambda\Lambda\eta_8} &= -\tfrac{2}{\sqrt{3}}(1 - \alpha)f, & f_{\Xi\Sigma K} &= -f.
\end{aligned}
\qquad (4)
$$

Accordingly, all coupling constants are given in terms of $f \equiv g_A/2f_0$ and the ratio $\alpha = F/(F + D)$. Here, f_0 is the Goldstone boson decay constant, g_A is the axial-vector strength measured in neutron β-decay, and $F + D = g_A$. Note that we will take the physical values of these various parameters, though strictly speaking in the effective Lagrangian they appear with their values in the chiral limit. This difference can be absorbed in higher order terms. In the present calculation, deviations of the meson-baryon coupling constants from the SU(3) values are taken into account. Specifically, there is an explicit SU(3) symmetry breaking in the empirical values of the decay constants [48],

$$
\begin{aligned}
f_\pi &= 92.4\,\mathrm{MeV}, \\
f_K &= (1.19 \pm 0.01)f_\pi, \\
f_\eta &= (1.30 \pm 0.05)f_\pi.
\end{aligned}
\qquad (5)
$$

The somewhat smaller SU(3) breaking in the axial-vector coupling constants, see the pertinent discussion in Appendix B of Ref. [38], is neglected in the present study. However, following the practice in chiral NN potentials, we use $g_A = 1.29$, which is slightly larger than the experimental value, in order to account for the Goldberger–Treiman discrepancy. As before in [38], for the $F/(F + D)$ ratio, we adopt $\alpha = 0.4$ which is the SU(6) value. Further, the η meson is identified with the octet-state η_8. The isospin factors $\mathcal{I}_{B_1 B_2 \to B_3 B_4}$ are summarized in Table 1.

In the NN case, where only pion exchanges are taken into account, cutoff values in the range $\Lambda = 350$–550 MeV were considered where $\Lambda = 450$ MeV yields the best results [31]. The choice of the cutoff mass for the YN interaction is more delicate. On the one hand, we want to preserve the principal features of the underlying approximate SU(3) flavor symmetry, in particular the explicit SU(3) breaking in the long-range part of the potential due to the mass splitting between the pseudoscalar mesons π, K, and η. Since the kaon mass is around 495 MeV it seems appropriate to use cutoff masses that are at least 500 MeV, so that the essential role of the K meson for the YN dynamics can be incorporated. At the other end, large values, say 650 MeV or beyond, lead to highly non-perturbative potentials and bear the risk of the appearance of spurious bound states, according to the experience from NN studies [49]. Considering that aspect implicates that two-meson exchange contributions involving a K and/or η (πK, KK, etc.), where then the combined masses exceed the cutoff value, will be strongly suppressed. Therefore, there is no point to include them explicitly. Rather their effect should be subsumed into the contact terms. Thus, contrary to our earlier work [38,39], we expect and allow for SU(3) symmetry breaking of the LECs in the ΛN and ΣN systems. In this context, it should be mentioned that also the counterterms in Eq. (1) constitute effectively an SU(3) symmetry breaking contact interaction.

In the present work we consider the cutoff values $\Lambda = 500$, 550, and 600 MeV. Clearly, for the lowest value η

Table 1 Isospin factors $\mathcal{I}$ for the various one–pseudoscalar-meson exchanges

	Channel	Isospin	π	K	η
$S = 0$	$NN \to NN$	0	-3	0	1
		1	1	0	1
$S = -1$	$\Lambda N \to \Lambda N$	$\frac{1}{2}$	0	1	1
	$\Lambda N \to \Sigma N$	$\frac{1}{2}$	$-\sqrt{3}$	$-\sqrt{3}$	0
	$\Sigma N \to \Sigma N$	$\frac{1}{2}$	-2	-1	1
		$\frac{3}{2}$	1	2	1

exchange will be already strongly suppressed and, in fact, we neglected its contribution in this case. The highest value is well above the masses of the K- and η mesons so that the effect of the SU(3) symmetry breaking in the masses of the pseudoscalar mesons on the YN interaction is well accounted for. In the discussion below we focus predominantly on the results for $\Lambda = 550$ MeV. However, some results, notably the χ^2, the effective range parameters and the hypertriton and $A = 4$ separation energies will be given for all three cutoffs in order to provide an overview of the quality of our chiral YN interactions. Anticipating the results, we stress that an equally good description of the considered YN, YNN and $A = 4$ hyper-nuclear observables can be achieved for all three cutoffs.

At leading order (LO), only a very basic description of the YN interaction can be obtained [34]. In particular, unrealistic small scattering lengths emerge from fits to the low-energy data under the prerequisite that the lightest Λ hypernuclei are not too strongly bound. Nonetheless, we construct also a LO interaction in the present study because we want to perform an uncertainty estimate of our chiral YN potentials following the procedure proposed in Ref. [45]. It turns out that under the assumption of SU(3) symmetry (note that SU(3) breaking contact terms arise first at NLO [50]) a LO fit with a decent χ^2 is only possible for a cutoff of $\Lambda = 700$ MeV and without subtraction. For smaller cutoffs, the χ^2 increases dramatically. We use that potential for the uncertainty estimate below but do not discuss its result in detail. Anyway, the LO results ($\chi^2 \approx 30$, $a_s^{\Lambda N} = -2.1$ fm, $a_t^{\Lambda N} = -1.2$ fm) are very similar to those based on a non-local cutoff reported in Ref. [34].

2.2 Contact terms

The spin dependence of the potentials due to the LO contact terms is given by [26]

$$V_{BB \to BB}^{(0)} = C_S + C_T\, \boldsymbol{\sigma}_1 \cdot \boldsymbol{\sigma}_2, \tag{6}$$

where the parameters C_S and C_T are low-energy constants (LECs) depending on the considered baryon-baryon channel.

These need to be determined by a fit to data. At NLO the spin- and momentum-dependence of the contact terms reads

$$
\begin{aligned}
V_{BB \to BB}^{(2)} =\ & C_1 \mathbf{q}^2 + C_2 \mathbf{k}^2 + (C_3 \mathbf{q}^2 + C_4 \mathbf{k}^2)\, \boldsymbol{\sigma}_1 \cdot \boldsymbol{\sigma}_2 \\
& + \frac{i}{2} C_5 (\boldsymbol{\sigma}_1 + \boldsymbol{\sigma}_2) \cdot (\mathbf{q} \times \mathbf{k}) + C_6 (\mathbf{q} \cdot \boldsymbol{\sigma}_1)(\mathbf{q} \cdot \boldsymbol{\sigma}_2) \\
& + C_7 (\mathbf{k} \cdot \boldsymbol{\sigma}_1)(\mathbf{k} \cdot \boldsymbol{\sigma}_2) + \frac{i}{2} C_8 (\boldsymbol{\sigma}_1 - \boldsymbol{\sigma}_2) \cdot (\mathbf{q} \times \mathbf{k})
\end{aligned}
\tag{7}
$$

where the C_i ($i = 1, \ldots, 8$) are additional LECs and $\mathbf{k}$ is the average momentum defined by $\mathbf{k} = (\mathbf{p}' + \mathbf{p})/2$. When performing a partial-wave projection, these terms contribute to the two S–wave ($^1S_0$, $^3S_1$) potentials, the four P–wave ($^1P_1$, $^3P_0$, $^3P_1$, $^3P_2$) potentials, and the $^3S_1$-$^3D_1$ and $^1P_1$-$^3P_1$ transition potentials in the following way [44] (note that due to the absence of the Pauli principle, there is one more term than in the NN case):

$$V(^1S_0) = \tilde{C}_{1S_0} + C_{1S_0}(p^2 + p'^2), \tag{8}$$

$$V(^3S_1) = \tilde{C}_{3S_1} + C_{3S_1}(p^2 + p'^2), \tag{9}$$

$$V(^3D_1 - {}^3S_1) = C_{3SD_1}\, p'^2, \tag{10}$$

$$V(^3S_1 - {}^3D_1) = C_{3SD_1}\, p^2, \tag{11}$$

$$V(^3P_0) = C_{3P_0}\, p\, p', \tag{12}$$

$$V(^1P_1) = C_{1P_1}\, p\, p', \tag{13}$$

$$V(^3P_1) = C_{3P_1}\, p\, p', \tag{14}$$

$$V(^3P_1 - {}^1P_1) = C_{3P_1 - {}^1P_1}\, p\, p', \tag{15}$$

$$V(^1P_1 - {}^3P_1) = C_{1P_1 - {}^3P_1}\, p\, p', \tag{16}$$

$$V(^3P_2) = C_{3P_2}\, p\, p', \tag{17}$$

with $p = |\mathbf{p}|$ and $p' = |\mathbf{p}'|$. $\tilde{C}_\alpha$ and C_α are appropriate combinations of the C_i's appearing in Eqs. (6) and (7), see Ref. [38].

Assuming only isospin symmetry, the LECs for each spin-isospin state of the $BB \to BB$ potentials are independent. When imposing SU(3) flavor symmetry one obtains relations between the LECs in the strangeness $S = 0$ and $S = -1$ systems, see Table 2, so that the total number of independent terms is noticeably reduced [38]. Specifically, for the partial waves relevant at low energies, $^1S_0$ and $^3S_1$, within SU(3) symmetry there are only 10 independent LECs (5 at

Table 2 SU(3) relations for the interactions in different $B_1 B_2 \to B_3 B_4$ channels, with isospin I and strangeness S. C_ξ^{27} etc. refers to the corresponding irreducible SU(3) representation for a particular partial wave ξ [34,38]

	Channel	I	$V(\xi)$		
			$\xi = {}^1S_0, {}^3P_0, {}^3P_1, {}^3P_2$	$\xi = {}^3S_1, {}^3S_1-{}^3D_1, {}^1P_1$	$\xi = {}^1P_1-{}^3P_1$
$S = 0$	$NN \to NN$	0	–	C_ξ^{10*}	–
	$NN \to NN$	1	C_ξ^{27}	–	–
$S = -1$	$\Lambda N \to \Lambda N$	$\frac{1}{2}$	$\frac{1}{10}\left(9C_\xi^{27} + C_\xi^{8_s}\right)$	$\frac{1}{2}\left(C_\xi^{8_a} + C_\xi^{10*}\right)$	$\frac{-1}{\sqrt{20}}C_\xi^{8_s 8_a}$
	$\Lambda N \to \Sigma N$	$\frac{1}{2}$	$\frac{3}{10}\left(-C_\xi^{27} + C_\xi^{8_s}\right)$	$\frac{1}{2}\left(-C_\xi^{8_a} + C_\xi^{10*}\right)$	$\frac{-3}{\sqrt{20}}C_\xi^{8_s 8_a}$
	$\Sigma N \to \Lambda N$				$\frac{1}{\sqrt{20}}C_\xi^{8_s 8_a}$
	$\Sigma N \to \Sigma N$	$\frac{1}{2}$	$\frac{1}{10}\left(C_\xi^{27} + 9C_\xi^{8_s}\right)$	$\frac{1}{2}\left(C_\xi^{8_a} + C_\xi^{10*}\right)$	$\frac{3}{\sqrt{20}}C_\xi^{8_s 8_a}$
	$\Sigma N \to \Sigma N$	$\frac{3}{2}$	C_ξ^{27}	C_ξ^{10}	–

LO and 5 at NLO) altogether, whereas with isospin symmetry alone there would be 16. Like in our previous studies [38,39], we impose SU(3) constraints on the LECs. However, for the reasons discussed above, those constraints are relaxed in the course of the fitting procedure whenever required for improving the description of the Λp and ΣN low-energy data. In practice, a departure from SU(3) symmetry is only necessary for the LO S-wave LECs, which is anyway in line with the employed power counting, see Refs. [38] (Appendix B) and [50].

Note that we do not consider the possible ${}^1P_1$-${}^3P_1$ transition at the present stage. In principle, one could fix the pertinent LECs which correspond to an antisymmetric ΛN-ΣN spin-orbit force, c.f. the term involving C_8 in Eq. (7), by considering the Scheerbaum factor [51] in nuclear matter as done by us in Refs. [52,53]. However, we intend to extend our calculations of Λ-hypernuclei within the NCSM approach [22,25] up to $A = 9$ systems in the future. Then we can directly use the empirical information on the level splitting of the ${}^9_\Lambda$Be hypernucleus [54] to investigate the strength needed for the elementary antisymmetric spin-orbit force.

2.3 Scattering equation

Once the YN potential is established, a partial-wave projection is performed [34] and the (ΛN or ΣN) reaction amplitudes are obtained from the solution of a coupled-channel Lippmann–Schwinger (LS) equation,

$$T_{\nu''\nu'}^{\ell''\ell',J}(p'', p'; \sqrt{s}) = V_{\nu''\nu'}^{\ell''\ell',J}(p'', p') $$
$$+ \sum_{\ell,\nu} \int_0^\infty \frac{dp\,p^2}{(2\pi)^3} V_{\nu''\nu}^{\ell''\ell,J}(p'', p)$$
$$\times \frac{2\mu_\nu}{k_\nu^2 - p^2 + i\eta} T_{\nu\nu',J}^{\ell\ell',J}(p, p'; \sqrt{s}). \quad (18)$$

The label ν indicates the channels and the label ℓ the partial wave. μ_ν is the pertinent reduced mass. The on-shell momentum in the intermediate state, k_ν, is defined by $\sqrt{s} = \sqrt{m_{B_{1,\nu}}^2 + k_\nu^2} + \sqrt{m_{B_{2,\nu}}^2 + k_\nu^2}$. Relativistic kinematics is used for relating the laboratory momentum p_{lab} of the hyperons to the c.m. momentum. For evaluating phase shifts, the LS equation is solved in the isospin basis. For observables, all calculations are performed in the particle basis, so that the correct physical thresholds can be incorporated. The Coulomb interaction (in the $\Sigma^- p$ and $\Sigma^+ p$ channels) is taken into account appropriately via the Vincent-Phatak method [61].

3 Results

In fitting to the YN data we proceed as before [38,39], i.e. we consider the set of 36 data for Λp, $\Sigma^- p$ and $\Sigma^+ p$ scattering at low energies [55–60] for determining the LECs in the S-waves. And, like before, as additional constraint, we require the hypertriton to be bound, which enables us to fix the relative strength of the singlet- and triplet S-waves in the Λp channel, see Sect. 3.4 for more details. SU(3) symmetry is imposed for the contact terms at the initial stage but eventually relaxed for the LO LECs, $\tilde{C}_{1S_0}$ and $\tilde{C}_{3S_1}$ in Eqs. (8,11), in line with the power counting where SU(3) breaking terms arise from mass insertions in the chiral Lagrangian at the NLO level [50]. Anyway, as said, we do expect some SU(3) breaking in the contacts terms in view of the fact that two-meson exchange contributions from πK, $\pi \eta$, etc. are not explicitly included. The achieved χ^2 is comparable to the one found for our NLO interactions [38,39], and typically around 16 for the 36 data points, see Table 3. An overview of the scattering lengths and effective ranges for the various YN channels is provided in Table 4. Preliminary results have been reported in Ref. [62].

Table 3 Comparison between the 36 YN data and the theoretical results for the various cutoffs in terms of the achieved χ^2. The last two columns are results for the NLO13 [38] and NLO19 [39] YN potentials

Λ (MeV)	Data	SMS NLO			SMS N²LO			NLO13	NLO19
		500	550	600	500	550	600	600	600
$\Lambda p \to \Lambda p$	Sechi-Zorn [55]	1.8	1.6	1.5	1.9	1.9	1.8	1.4	1.9
	Alexander [56]	2.2	2.5	2.7	2.0	2.1	2.2	3.0	1.6
$\Sigma^- p \to \Lambda n$	Engelmann [57]	3.6	3.8	4.0	3.6	4.0	3.6	4.1	4.0
$\Sigma^- p \to \Sigma^0 n$	Engelmann [57]	5.9	5.8	5.8	5.9	5.9	5.9	5.8	6.0
$\Sigma^- p \to \Sigma^- p$	Eisele [58]	1.9	1.8	1.8	2.0	1.9	1.9	1.9	2.2
$\Sigma^+ p \to \Sigma^+ p$	Eisele [58]	0.1	0.3	0.4	0.2	0.2	0.3	0.5	0.4
r_R	[59,60]	0.1	0.0	0.0	0.3	0.1	0.1	0.1	0.1
total χ^2		15.5	15.7	16.2	15.8	15.6	15.7	16.8	16.3

Table 4 Scattering lengths (a) and effective ranges (r) for singlet (s) and triplet (t) S-waves (in fm), for ΛN, ΣN with isospin $I = 1/2$, $3/2$, and for $\Sigma^+ p$ with inclusion of the Coulomb interaction

Λ [MeV]	SMS NLO			SMS N²LO			NLO13	NLO19
	500	550	600	500	550	600	600	600
$a_s^{\Lambda N}$	-2.80	-2.79	-2.79	-2.80	-2.79	-2.80	-2.91	-2.91
$r_s^{\Lambda N}$	2.87	2.72	2.63	2.82	2.89	2.68	2.78	2.78
$a_t^{\Lambda N}$	-1.59	-1.57	-1.56	-1.56	-1.58	-1.56	-1.54	-1.41
$r_t^{\Lambda N}$	3.10	2.99	3.00	3.16	3.09	3.17	2.72	2.53
$\mathrm{Re}\, a_s^{\Sigma N\ (I=1/2)}$	1.14	1.15	1.10	1.03	1.12	1.06	0.90	0.90
$\mathrm{Im}\, a_s^{\Sigma N}$	0.00	0.00	0.00	0.00	0.00	0.00	0.00	0.00
$\mathrm{Re}\, a_t^{\Sigma N\ (I=1/2)}$	2.58	2.42	2.31	2.60	2.38	2.53	2.27	2.29
$\mathrm{Im}\, a_t^{\Sigma N}$	-2.60	-2.95	-3.09	-2.56	-3.26	-2.64	-3.29	-3.39
$a_s^{\Sigma N\ (I=3/2)}$	-4.21	-4.05	-4.11	-4.37	-4.19	-4.03	-4.45	-4.55
$r_s^{\Sigma N}$	3.93	3.89	3.75	3.73	3.89	3.74	3.68	3.65
$a_t^{\Sigma N\ (I=3/2)}$	0.46	0.47	0.47	0.38	0.44	0.41	0.44	0.43
$r_t^{\Sigma N}$	-5.08	-4.74	-4.82	-5.70	-4.96	-5.72	-4.59	-5.27
$a_s^{\Sigma^+ p}$	-3.41	-3.30	-3.44	-3.47	-3.39	-3.25	-3.56	-3.62
$r_s^{\Sigma^+ p}$	3.75	3.73	3.59	3.61	3.73	3.65	3.54	3.50
$a_t^{\Sigma^+ p}$	0.51	0.52	0.52	0.41	0.48	0.45	0.49	0.47
$r_t^{\Sigma^+ p}$	-5.46	-5.12	-5.19	-6.74	-5.50	-6.41	-5.08	-5.77

In the detailed discussion of the results, we focus on the ones for the cutoff 550 MeV. Those for the other considered cutoffs, 500 and 600 MeV, are very similar as one can conjecture from the χ^2 values. Also, we start with the ΣN channels where new data from the J-PARC E40 experiment have become available [7–9]. Here, $\Sigma^+ p$ scattering is of particular interest for theory since it is a pure isospin $I = 3/2$ system. Thus, there is no coupling to the ΛN channel which simplifies the dynamics. Moreover, there are, in principle, rather restrictive constraints from SU(3) symmetry. Specifically, the space-spin antisymmetric states ($^1S_0$, $^3P_{0,1,2,...}$) belong all to the {27} irrepresentation (irrep) of SU(3) (cf. Table 2) [38,39] and thus the corresponding interactions would be identical to those in the NN system provided that SU(3) symmetry is exactly fulfilled. While there is a sizable SU(3) symmetry breaking in case of the $^1S_0$ partial wave [63], the amplitudes in the P- and higher partial waves could be much closer to those found for NN scattering.

Note that the cross sections in the $\Sigma^+ p \to \Sigma^+ p$ and $\Sigma^- p \to \Sigma^- p$ channels in past studies were obtained from experiments with an incomplete angular coverage by defining [58]
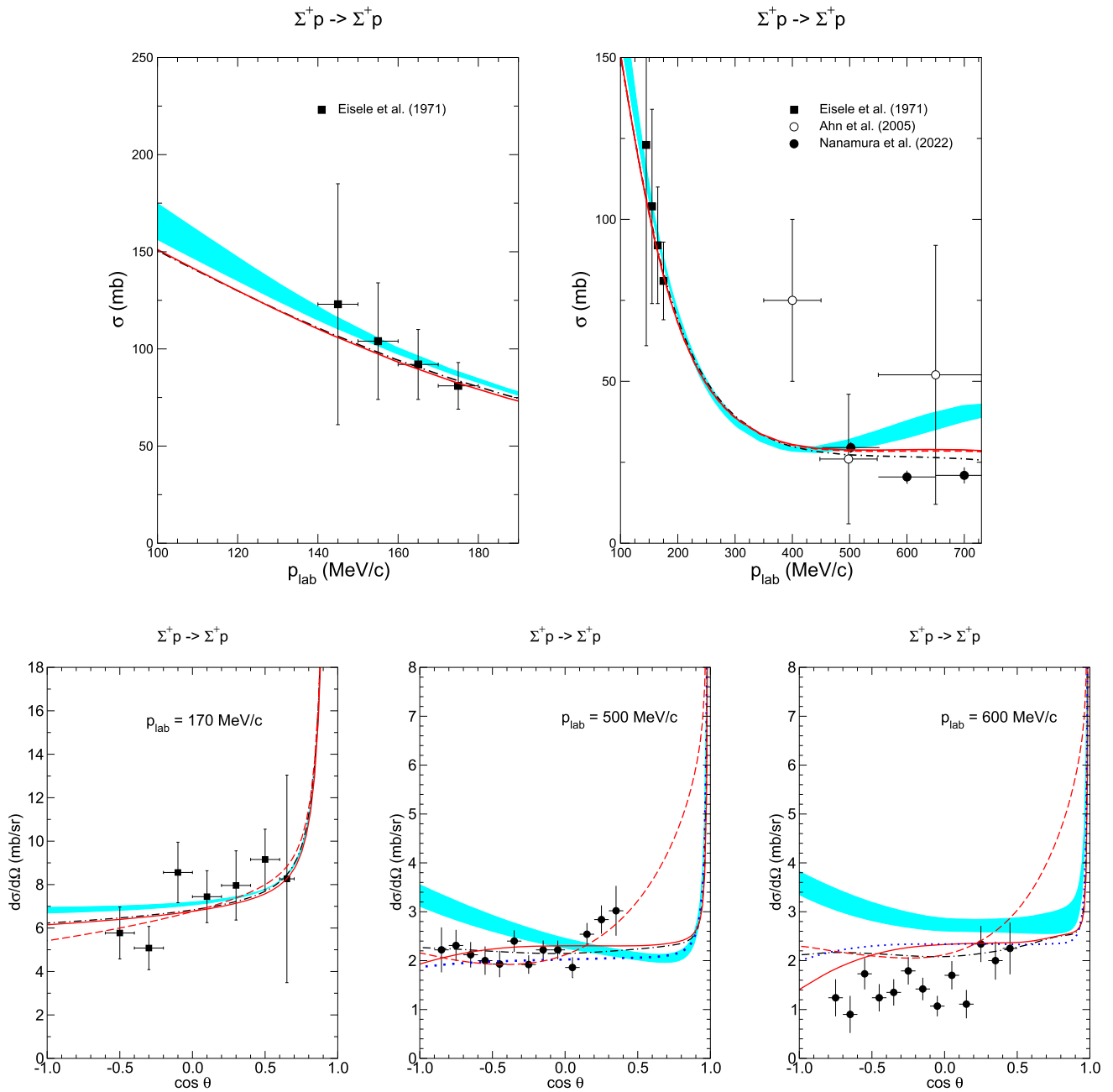
Fig. 1 Cross section for $\Sigma^+ p$ scattering as a function of p_{lab}. Results are shown for the SMS NLO (dash-dotted) and N^{2}LO (solid) YN potentials with cutoff 550 MeV. The dashed line corresponds to an alternative fit at N^{2}LO, see text. The cyan band is the result for NLO19 [39]. The dotted line is the result for NLO19 (600) with readjusted C_{3SD_1}, see text. Data are from the E40 experiment [9] for the momentum regions 440–550 and 550–650 MeV/c, respectively, and from Refs. [58,64]

$$\sigma = \frac{2}{\cos\theta_{max} - \cos\theta_{min}} \int_{\cos\theta_{min}}^{\cos\theta_{max}} \frac{d\sigma(\theta)}{d\cos\theta} d\cos\theta. \qquad (19)$$

We use the same prescription, and specifically $\cos\theta_{min} = -0.5$ and $\cos\theta_{max} = 0.5$, for obtaining "integrated" $\Sigma^+ p$ and $\Sigma^- p$ cross sections.

3.1 The $\Sigma^+ p$ channel

$\Sigma^+ p$ scattering cross sections for the SMS YN interactions are presented in Fig. 1, and compared with data and with the results obtained from the NLO19 potential. The latter are shown as bands, representing the cutoff dependence [39]. On the upper left side the cross section at low energies is

displayed. This is the region with the data of Eisele et al. [58], which are included in the fitting procedure for the S-wave LECs. One can see that the results for the SMS potentials are slightly below those of NLO19. The main reason for that is that we no longer impose strict SU(3) constraints on the S-wave contact terms.

Once the S-wave LECs are fixed from a combined fit to the Λp and ΣN cross sections, the differential cross sections established in the E40 experiment are analyzed. Interestingly, in the NLO case taking over the LECs from the corresponding NN potential by Reinert et al. [31] for the $^3P_{0,1,2}$ partial waves, in accordance with SU(3) symmetry, and assuming the LEC in the $^1P_1$ to be zero, yields already a good description of the E40 data in the region 440–550 MeV/c, cf. Figure 1 (center of the lower panel). For the N^{2}LO interaction all P-wave LECs are adjusted to the data. Actually, here we explore two scenarios (denoted by the superscripts a and b in the tables below so that one can distinguish them), one where the resulting angular distribution is similar to that obtained for NLO (solid line) and one which produces an overall more pronounced angular dependence (dashed line). The latter is clearly preferred by the available data in that momentum range. However, a view on the situation in the next momentum region, 550–650 MeV/c, see Fig. 1 (lower right), tells us that one has to be careful with conclusions. Here the experiment suggest an overall somewhat different angular dependence, which seems to be more in line with a flat behavior or a very moderate increase in forward direction. In any case, note that the alternative fit provides an at least visually slightly better description of the old low-energy data (lower left). Indeed, those data from the momentum region 160–180 MeV/c [58] ($T_{lab} \approx 12$ MeV) seem to exhibit a more pronounced angular dependence than the E40 data at much higher momenta. Thus, it would be very interesting to explore the energy region in between by experiments. Such data could also help to pin down the P-wave contributions more reliably since higher partial waves should be much less important. For completeness, let us mention that the fitting ranges considered for establishing the SMS NN potential are $p_{lab} \lesssim 480$ MeV/c at NLO and $p_{lab} \lesssim 540$ MeV/c at N^{2}LO [31].

The predictions by NLO19 are definitely at odds with the E40 experiment. However, it should be said that the pronounced rise of the cross section for backward angles, excluded by the data, is mainly due to an accidental choice of the LEC $C_{^3SD_1}$ in the ΣN $I = 3/2$ contact interaction in [38,39]. Its value can be easily re-adjusted, without any change in the overall quality of those YN potentials. Pertinent results, for NLO19(600) as example, are indicated by dotted lines in Fig. 1.

The integrated $\Sigma^+ p$ cross section over a larger energy range is shown in Fig. 1 (upper right). Note that again the angular averaging according to Eq. (19) is applied to the the-
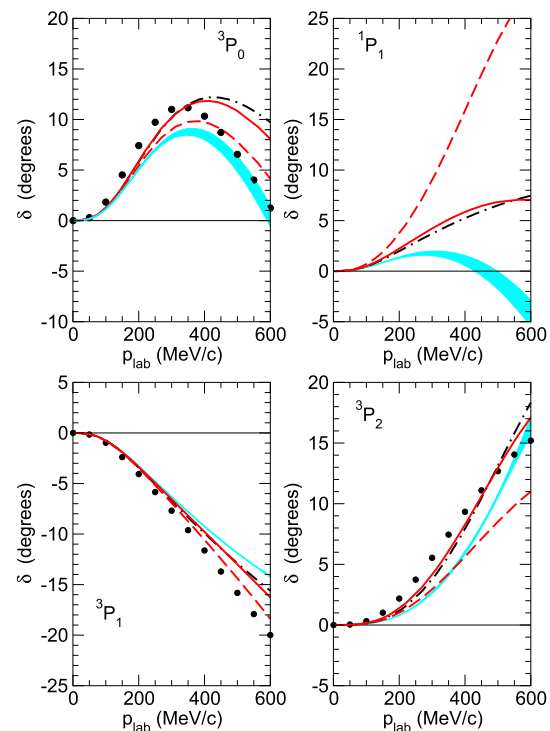

Fig. 2 ΣN $I = 3/2$ phase shifts: P-waves. Same description of the curves as in Fig. 1. For illustrating the extent of SU(3) symmetry breaking, NN phase shifts [65,66] for partial waves in the pertinent {27} irrep are indicated by circles

ory results. It is likewise done to obtain the indicated E40 data points because only differential cross sections in a limited angular range are available [9]. Once more the NLO19 potential does not reproduce the trend of the data. Specifically, contrary to the experiment, there is a rise of the cross section for larger p_{lab} which we observed also for NLO13 and which seems to be present also in results by the so-called covariant chiral EFT [35,37]. This rise is due to an artificial behavior of the $^3S_1$ partial wave, presumably caused by the non-local regulator employed in our NLO13 and NLO19 potentials. Anyway, since $p_{lab} = 600$ MeV/c corresponds to a laboratory energy of $T_{lab} \approx 150$ MeV, one is certainly in a region where NLO and possibly even N^{2}LO cannot be expected to be still quantitatively reliable. In this context, one should keep in mind that the $\Lambda N\pi$ channel opens around that energy which clearly marks the formal limit for the applicability of any effective two-body potential. However, whether the noticeable drop in the experimental cross section, which can not be reproduced by theory, has something to do with the opening of that channel or not, remains unclear at present.

The authors of Ref. [9] have attempted to perform a phase-shift analysis, including partial waves up to the total angular momentum of $J = 2$, with the aim to determine the phase in the $^3S_1$ channel. For that different scenarios have been considered where the phase shifts in the partial waves in the
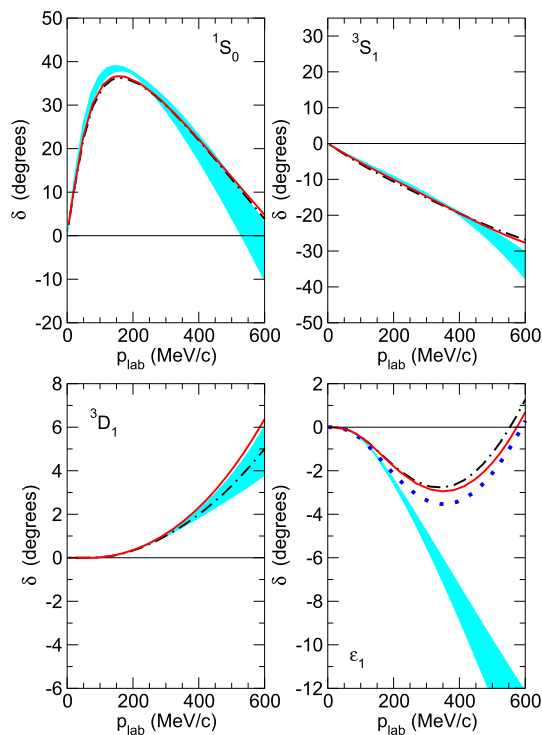
Fig. 3 ΣN $I = 3/2$ phase shifts: $^1S_0$ and $^3S_1$–$^3D_1$. Same description of the curves as in Fig. 1

{27} irrep of SU(3), cf. Table 2, were fixed either from NN results (exploiting SU(3) symmetry) or from predictions of YN models. Earlier efforts for establishing the ΣN $I = 3/2$ phase shifts, based on the differential cross section of Eisele et al. (lower-left of Fig. 1), can be found in Refs. [72,73]. Our predictions for the phase shifts are displayed in Figs. 2 and 3. For illustration we include the NN phase shifts in the $^3P_{0,1,2}$ partial waves (circles) which, as said, would be identical to the ones for ΣN with $I = 3/2$ under strict validity of SU(3) symmetry. It is interesting to see that the difference is indeed fairly small. In comparison, the predictions of the chiral potentials for $^1P_1$, not constrained by SU(3), vary sizably. The results for the $^1S_0$ and $^3S_1$ partial waves shown in Fig. 3 are, of course, strongly constrained by the available low-energy cross section data. The behavior of the $^1S_0$ is qualitatively similar to that in the NN case [31], as expected from the approximate SU(3) symmetry. One can observe a large difference in the results for the mixing angle ϵ_1 between the SMS YN potentials and NLO19. As discussed above, its large value is the reason for the rise of the cross section at backward angles, cf. Fig. 1. At the time when NLO19 and NLO13 were established, the existing data did not allow to fix the relevant LEC ($C_{^3SD_1}$) reliably. However, it can be re-adjusted (see the dotted line) without changing the overall χ^2 and then the pertinent results can be brought in line with the E40 measurement.

3.2 The $\Sigma^- p$ channel

Results for $\Sigma^- p$ elastic scattering are presented in Fig. 4. The SMS YN potentials produce a slightly weaker energy dependence of the integrated cross section than NLO19. In the momentum region of the new E40 data [7], $p_{lab} = 500$–700 MeV/c, the predictions of all our YN potentials are similar and in agreement with the experiment. Also the differential cross sections agree with the experiment, cf. the lower panel of Fig. 4. It should be said, however, that the proper behavior in forward direction remains somewhat unclear since the experimental information is too sparse in that angular region. Nonetheless, the data points available for the momentum region 550–650 MeV/c could point to a somewhat steeper rise for small angles. The predictions based on NLO19 exhibit a sizable cutoff dependence. It is due to the fact that the hadronic amplitude is overall attractive for some cutoffs and repulsive for others so that there is either a destructive or constructive interference with the attractive Coulomb interaction. In case of a destructive interference there is a small dip in the differential cross section at very forward angles. Data with high resolution would be needed in order to resolve that issue.

Results for the transition $\Sigma^- p \rightarrow \Lambda n$ are presented in Fig. 5. Also in this case the predictions of the SMS YN potentials and those of NLO19 are rather similar. Specifically, all interactions yield a reaction cross section in line with the E40 data [8]. The angular distributions are likewise reproduced, cf. Fig. 5 (center and left of the lower panel). One should keep in mind that in case of NLO19 no actual fitting of the P-wave LECs was performed. The ones belonging to the {27} and {10*} irreps were taken over from fits to NN P-waves, exploiting SU(3) symmetry constraints, whereas the others were fixed qualitatively by requiring that the contribution of each P-wave to the Λp cross section for momenta above the ΣN threshold remains small [38]. We note that for $\Sigma^- p \rightarrow \Lambda n$ partial waves up to $J = 8$ are needed to achieve converged results for the differential cross section at 600 MeV/c.

In the context of the inelastic $\Sigma^- p$ data by Engelmann et al. [57], we would like to point to a footnote in that paper which emphasizes the role of the Σ^- lifetime in their determination of the cross sections. The fact that the present value is almost 10 % smaller [74] suggests that the actual cross sections could be smaller, too.

There are no new data for the charge-exchange reaction $\Sigma^- p \rightarrow \Sigma^0 n$. The predictions of chiral EFT are in agreement with the existing experimental evidence, as one can see in Fig. 6.
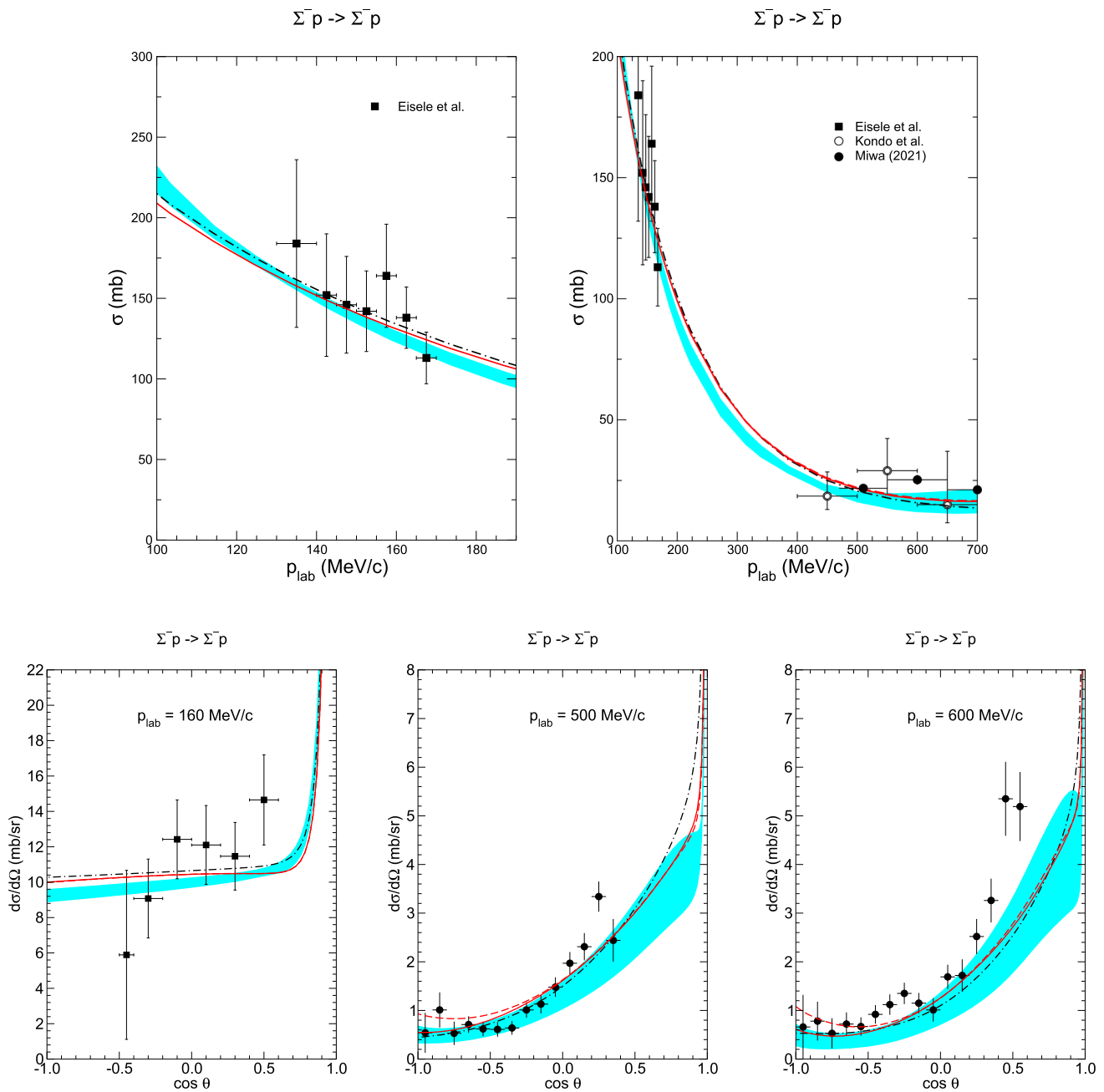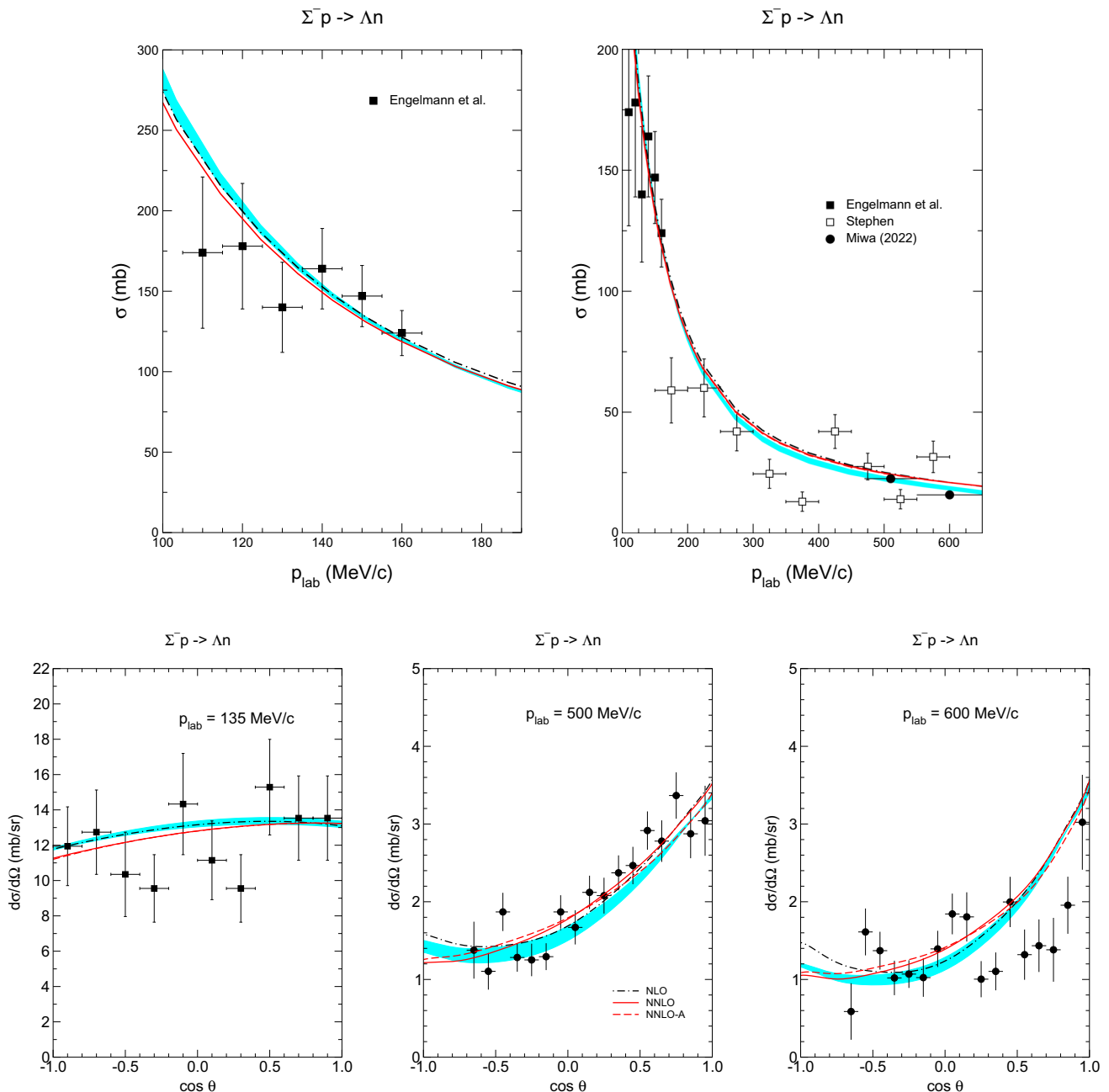
Fig. 4 Cross section for $\Sigma^- p$ scattering as a function of p_{lab}. Same description of the curves as in Fig. 1. Data are from the E40 Collaboration [7] for the momentum regions 470–550 and 550–650 MeV/c, respectively, and from Refs. [58,67]

3.3 The Λp channel

Results for Λp scattering are presented in Fig. 7. So far there are no data from J-PARC for this channel. The new Λp data from CLAS/Jlab [6] are at fairly high momenta ($p_{lab} \geq 900$ MeV/c) so that a quantitative comparison with our NLO and N²LO predictions is not really sensible. Nonetheless, we display the momentum region up to their lowest data point (inverted triangle) so that one can see that the trend of our predictions is well in line with that mea-

surement. Anyway, the low-energy data are reproduced with similar quality by all chiral potentials, as expected in view of the excellent and low χ^2 achieved in all fits. It is interesting though that even the predicted cusp at the ΣN threshold is practically identical, cf. Fig. 7 (upper right). This testifies that the actual shape of the cusp is to a large extent determined by the ΣN low-energy data [75] which, of course, are all described well by the considered YN potentials as discussed above.

Fig. 5 Cross section for $\Sigma^- p \to \Lambda n$ as a function of p_{lab}. Same description of the curves as in Fig. 1. Data are from the E40 Collaboration [8] for the momentum regions 470–550 and 550–650 MeV/c, respectively, and from Refs. [57,60]

There are no genuine differential cross sections available for Λp scattering. However, some data on the angular distribution and the forward/backward ratio can be found in Refs. [55,56]. Those are shown in the lower panel of Fig. 7 and compared with predictions normalized to the number of events. Evidently, all our chiral potentials predict the trend of the data that indicate a rise of the cross section in forward direction. The present data would favor a more pronounced angular dependence as produced by one of the N²LO inter-

actions (solid line). But for a quantitative conclusion more accurate data are needed. Also measurements for somewhat higher momenta, closer to the ΣN thresholds, would be quite instructive [39]. Such data are expected to be provided by the future E86 experiment at J-PARC [42].

Results for ΛN phase shift in the S- and P-waves are shown in Figs. 8 and 9. Like in case of ΣN discussed above, the predictions for the $^1S_0$ and $^3S_1$ partial waves are strongly constrained by fitting the cross section data. And,

Fig. 6 Cross section for $\Sigma^- p \to \Sigma^0 n$ as a function of p_{lab}. Same description of the curves as in Fig. 1. Data are from Refs. [57,60]
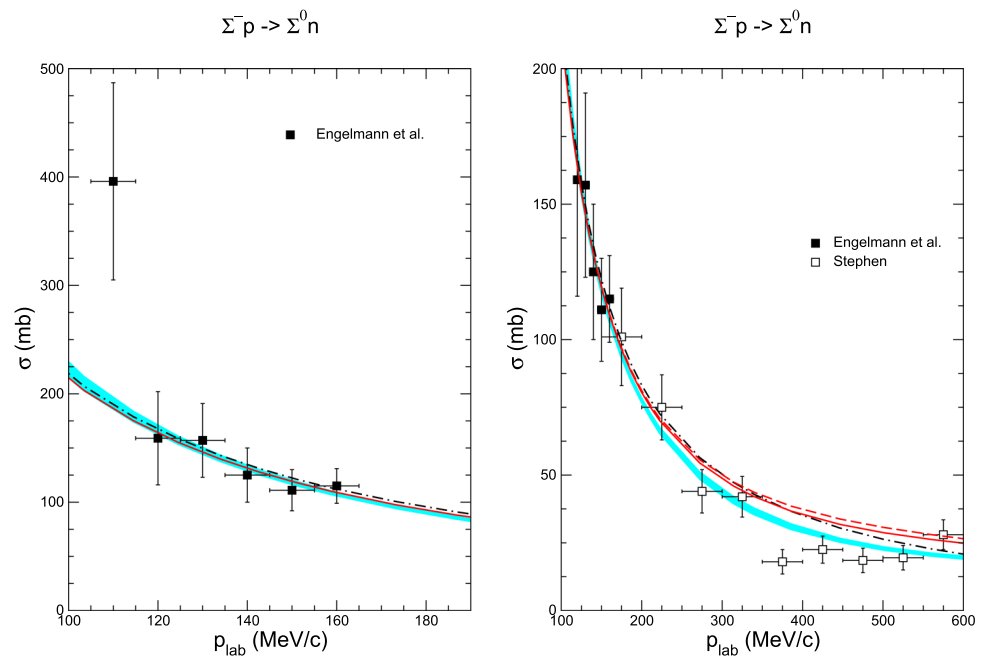
as already mentioned, like in our previous works [38,39,76] the empirical binding energy of the hypertriton $^3_\Lambda$H is used as a further constraint. Thereby we can exploit the fact that the spin-singlet and triplet amplitudes contribute with different weights to the Λp cross section and to the $^3_\Lambda$H binding energy, see Eq. (9) in [39]. Without that feature it would not be possible to fix the relative strength of the spin-singlet and spin-triplet S-wave components of the Λp interaction. A more detailed discussion on the hypertriton will be provided in the next subsection. However, we want to mention already here that we fixed the strength in the spin-singlet interaction based on some exploratory calculations with SMS NLO (550). The resulting scattering length, $a_s \approx -2.80$ fm, was then used to adjust all other NLO and N^{2}LO interactions. This value is slightly smaller in magnitude that what has been found and used for the NLO13 and NLO19 interactions with non-local cutoff, see Table 4. Nonetheless, the chiral YN interactions with the new regularization scheme tend to be overall slightly more attractive. This is best seen in Fig. 8 from the $^1S_0$ phase shifts, where the predictions by the SMS potentials drop off more slowly with increasing momentum as compared to those of our former YN interactions.

As discussed in Ref. [75], most of the YN potentials, that include the ΛN-ΣN coupling and provide a quantitative description of the data, predict an unstable ΣN bound state near the ΣN threshold. This is reflected in the behavior of the $^3S_1$-$^3D_1$ phase shifts, where either the $^3S_1$ or $^3D_1$ phase pass through 90° [34,38]. In case of the SMS potentials this happens in the $^3D_1$ state. Note that for convenience, and to keep the scales of the figures commensurable, we show the results in Fig. 8 modulo 180°.

The results for the P-waves are qualitatively rather similar, except for the $^1P_1$ where the NLO19 prediction is of opposite sign. Certainly, the ^3P states are all dominated by the {27} irrep of SU(3) (Table 2) and, thus, strongly constrained by fixing the pertinent LECs in a fit to the NN phases (in case of NLO19 and SMS NLO) and to the new $\Sigma^+ p$ data (in the SMS N^{2}LO YN potentials). It will be interesting to see whether those predictions are consistent with Λp differential cross sections, once such data become available from J-PARC [42].

Recently, the Λp two-particle momentum correlation function has been measured with high precision by the ALICE Collaboration in pp collisions at 13 TeV [12]. An exploratory analysis of those data suggests that the Λp interaction could be slightly less attractive than what follows from the low-energy Λp cross section data [55,56]. However, since additional ingredients and parameters are required for a more detailed evaluation [77–79], those data cannot be included straightforwardly into our fitting procedure. Therefore, we refrain from taking into account constraints provided by such correlation functions at the present stage.

Finally, we want to mention that there are data for the Λ polarization, $\alpha \bar{P}(\theta^*_\Lambda)$, for forward and backward angles, see Table II of Ref. [56]. α is the weak decay parameter of the Λ [74]. These suggest that the polarization is practically consistent with zero for $p_{lab} \leq 320$ MeV/c. Since the experimental uncertainties are rather large, we do not display these data here. However, we want to mention that the results of the SMS potentials for αP in that momentum region are all smaller than 0.1. Also, we would like to point to Ref. [42] where results of NLO13 and NLO19 for the Λp analyzing
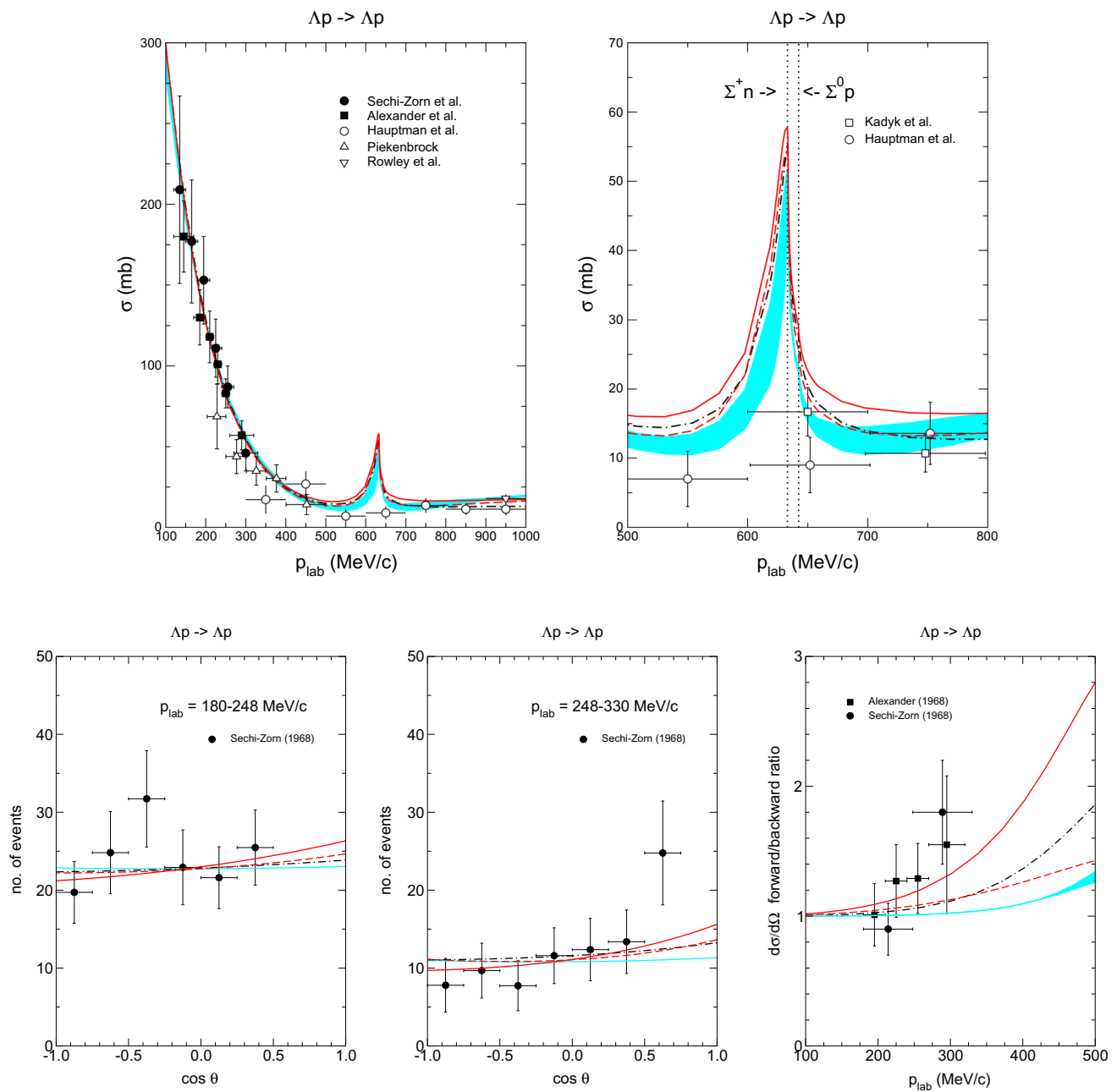
Fig. 7 Cross section for Λp as a function of p_{lab}. Same description of the curves as in Fig. 1. Data are from Refs. [55] (filled circles), [56] (filled squares), [68,69] (open triangles), [70] (open squares), [71] (open circles) and [6] (inverted triangles)

power are shown, and where one can see that those predictions are likewise rather small at low momenta.

3.4 $A = 3$ and $A = 4$ Λ hypernuclei

The binding energy of the hypertriton is obtained by solving Faddeev equations in momentum space. This method is well suited for the chiral YN and NN potentials which involve local as well as non-local components. A detailed description of the formalism can be found in [80,81]. In the discussion,

we focus on the separation energy which is the difference between the hypertriton binding energy and that of the core nucleus, i.e. that of the deuteron. As shown by us in Ref. [39], the Λ separation energies of light hypernuclei are not very sensitive to the employed NN interaction. Therefore, we use in all calculations the same state-of-the-art chiral NN interaction, namely the SMS NN potential of Ref. [31] at order N^{4}LO$^+$ with cutoff $\Lambda = 450$ MeV. The variation of the separation energy with the cutoff of the chiral NN potentials is only in the order of 10 keV, see Table 3 of Ref. [39]. Note
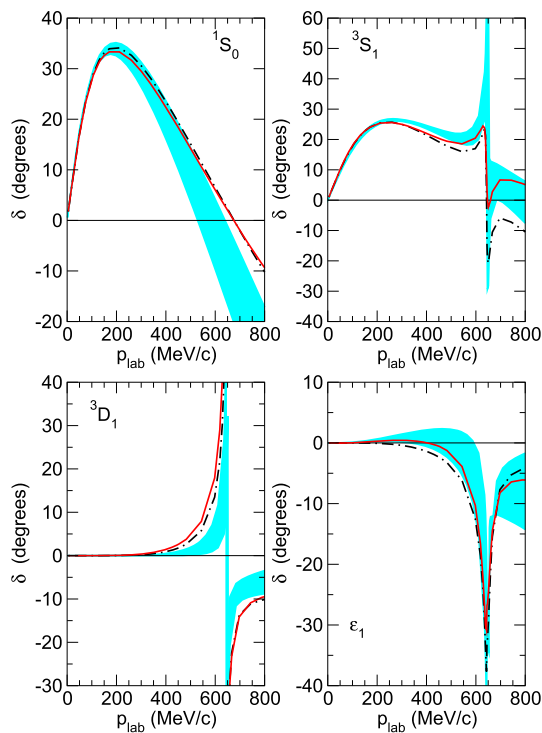
Fig. 8 ΛN phase shifts: $^1S_0$ and $^3S_1$–$^3D_1$. Same description of the curves as in Fig. 1. The results for the $^3S_1$ and $^3D_1$ phases are shown modulo 180°
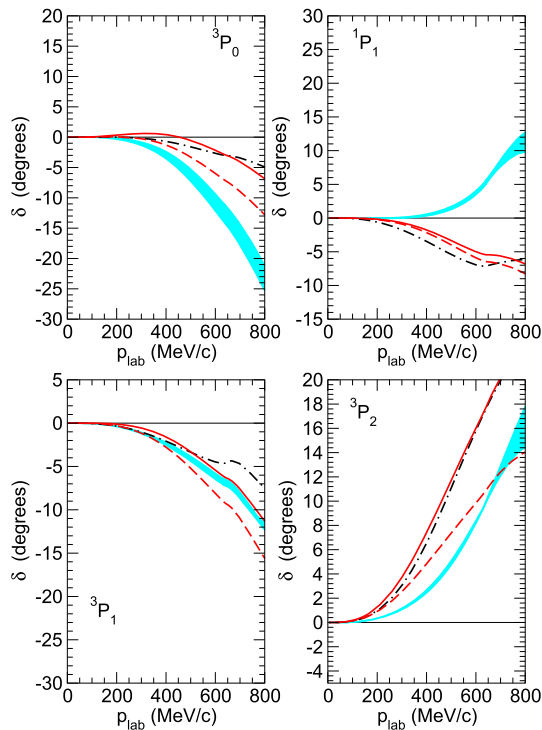

Fig. 9 ΛN phase shifts: P-waves. Same description of the curves as in Fig. 1

that some recent studies suggest a larger dependence on the NN potential [82,83]. This is in part due to using lower order NN interactions but also because the dependence on the NN interaction seems to be larger for the LO YN interactions. We are currently investigating the NN force dependence in more detail [84]. Our preliminary results confirm the small NN force dependence of the order of 10 keV for the NLO and N^{2}LO calculations presented here. The dependence is certainly much smaller than the experimental uncertainty of ±40 keV.

As already mentioned, we require the hypertriton to be bound as an additional constraint for our YN interaction. However, we do not include the $^3_\Lambda$H separation energy in the actual fitting procedure because of its large experimental uncertainty. While for a long time the value given by Jurič et al. [85], $B_\Lambda = 0.13 \pm 0.05$ MeV, has been accepted as the standard, recent measurements reported by the STAR and ALICE Collaborations indicate that the separation energy could be either significantly larger ($0.41 \pm 0.12 \pm 0.11$ MeV [14]) or somewhat smaller ($0.072 \pm 0.063 \pm 0.036$ MeV [15]). The latest average from the Mainz Group is 0.148 ± 0.040 MeV [86]. New high-precision experiments to determine the hypertriton binding energy are planned at the Mainz Microtron (MAMI) [86] and at JLab [87] and will hopefully resolve those discrepancies.

Given these variations, as a guideline of the present work, we aimed at achieving a $^3_\Lambda$H separation energy in the order of 150 keV with our chiral YN interactions. An arbitrary fine-tuning to one or the other value is not really meaningful at the present stage. It would be also questionable in view of the fact that there should be a contribution from chiral three-body forces (3BF) [43]. Those could contribute up to 50 keV to the binding, as argued in Ref. [39]. Incidentally, since the present experimental uncertainties exceed that estimation, there is no way of fixing the pertinent 3BF LECs from the hypertriton and, therefore, we refrain from including 3BFs in the present work. A possible and viable way to fix the 3BFs is, in our opinion, via studies of the $^4_\Lambda$H/$^4_\Lambda$He and $^5_\Lambda$He systems and we intend to explore that option in the future.

Results of the SMS YN potentials for the hypertriton separation energy are summarized in Table 5. It is interesting to see that the predicted values lie fairly close together, keeping in mind, of course, that the NLO and N^{2}LO potentials have been all tuned to the same ΛN scattering length in the $^1S_0$ partial wave. Evidently, the separation energies are well in line with the experimental values by Jurič et al. and agree also with the new ALICE measurement within the uncertainty. Compared to the previous chiral YN interactions NLO13 and NLO19, the separation energies are slightly larger indicating that the new interactions are more attractive than the previous ones.

It is now interesting to apply the same interactions to a more densely bound system, namely $^4_\Lambda$He. For this hypernu-

Table 5 Overview of results for the hypertriton up to N^{2}LO and for the Λ and Σ single-particle potentials in symmetric nuclear matter at saturation density

YN potential	B_Λ [MeV]	E [MeV]	P_Σ [%]	$U_\Lambda(0)$	$U_\Sigma(0)$
SMS LO(700)	0.135	−2.359	0.20	−37.8	10.2
SMS NLO(500)	0.127	−2.350	0.28	−30.1	0.2
SMS NLO(550)	0.124	−2.347	0.23	−32.1	−1.6
SMS NLO(600)	0.122	−2.345	0.32	−29.7	−3.1
SMS N^{2}LO(500)	0.147	−2.371	0.25	−33.1	6.4
SMS N^{2}LO(550)^a	0.139	−2.362	0.25	−38.5	2.5
SMS N^{2}LO(550)^b	0.125	−2.348	0.24	−35.9	2.5
SMS N^{2}LO(600)	0.172	−2.395	0.22	−37.8	0.1
NLO13(600)	0.090	−2.335	0.25	−21.6	17.1
NLO19(600)	0.091	−2.336	0.21	−32.6	16.9

The superscripts a and b denote the two variants introduced in Sect. 3.1 with different P-wave interactions. For the NN interactions SMS N^{4}LO$^+$(450) is used [31]. The NLO13 and NLO19 results are from [39]

Table 6 Overview of results for the $^4_\Lambda$He separation energy up to N^{2}LO

YN potential	$^4_\Lambda$He				
	$J^\pi = 0^+$			$J^\pi = 1^+$	
	B_Λ [MeV]	P_Σ [%]		B_Λ [MeV]	P_Σ [%]
SMS LO (700)	3.088	1.36		2.275	1.72
SMS NLO (500)	2.009	2.32		1.041	2.05
SMS NLO (550)	2.102	2.13		1.102	1.96
SMS NLO (600)	2.021	2.34		0.927	1.69
SMS N^{2}LO (500)	2.001	2.01		1.002	2.07
SMS N^{2}LO (550)^a	2.024	1.81		1.251	2.01
SMS N^{2}LO (550)^b	1.969	1.82		1.188	1.99
SMS N^{2}LO (600)	2.263	1.79		1.181	1.81
NLO13 (600)	1.477	2.02		0.580	1.51
NLO19 (600)	1.461	1.37		1.055	1.68

The superscripts a and b denote the two variants introduced in Sect. 3.1 with different P-wave interactions. For the NN interactions SMS N^{4}LO$^+$(450) [31] is used. For our new SMS results, we also apply the properly adjusted three-nucleon interaction (see [88]). The NLO13 and NLO19 results are from [39]

cleus, charge symmetry breaking (CSB) is expected to contribute of the order of 100 keV to the separation energies [89,90]. We do not include CSB terms here and likewise no YNN interactions since for now we are only interested in a first comparison with our previous calculations for NLO13 and NLO19. Without CSB interactions, the mirror hypernuclei $^4_\Lambda$He and $^4_\Lambda$H have very similar separation energies. Therefore, we only present results for $^4_\Lambda$He.

The binding energy for $A = 4$ hypernuclei are obtained by solving Yakubovsky equations in momentum space [81]. Such calculations require a large number of partial wave states for being converged. We have used here all partial waves with orbital angular momenta up to $l = 6$ and a sum of the three orbital angular momenta related to the three relative momenta necessary up 8. With this restriction of partial

waves, our accuracy is of the order of 50 keV for the separation energies.

The results are summarized in Table 6. It can be seen that the trend to larger separation energies applies also for $A = 4$. In particular, for the $J^\pi = 0^+$ ground state, the energies are now significantly closer to the experiment, where the current average value is 2.347 ± 0.036 MeV [91]. Also for the $J^\pi = 1^+$ excited state the predictions are close to the empirical value. Here the experimental average is 0.942 ± 0.036 MeV. In this case the separation energies are also similar to those obtained for the NLO19 interaction [39]. These results indicate that the state/spin dependence of ΛNN (and/or ΣNN) three-body forces should be different for the new series of interactions compared to NLO19 and NLO13. In any case it is interesting to see that the SMS interactions

lead to larger Σ probabilities than NLO19. In past calculations it was observed that such larger contributions of Σ's to the hypernuclear states usually lead to smaller binding energies, c.f. the comparison of NLO13 and NLO19.

3.5 Λ and Σ in nuclear matter

For completing the picture, we include results for the in-medium properties of the Λ and Σ based on the new YN interactions. Specifically, we provide the predictions for the single-particle potentials $U_Y(p_Y)$ at nuclear matter saturation density ($k_F = 1.35$ fm^{-1}), evaluated self-consistently within a conventional G-matrix calculation, utilizing the formalism described in detail in Refs. [39,52]. As one can see from Table 5, $U_\Lambda(p_\Lambda = 0)$ for the SMS YN potentials is around -30 to -38 MeV, while $U_\Sigma(p_\Sigma = 0)$ is around -3 to $+6$ MeV.

The predicted value for $U_\Lambda(0)$ is comparable to the result for NLO19 and also well in line with the usually cited empirical value of $U_\Lambda = -27 \sim -30$ MeV [92]. Thus, the conclusions drawn in Refs. [93,94] on the properties of neutron stars and a possible solution of the hyperon puzzle based on the NLO13 and NLO19 potentials remain unchanged. In that works it was argued that the combined repulsive effects of the two-body interaction and a chiral ΛNN three-body force could be sufficiently strong to prevent the appearance of Λ hyperons in neutron stars. We want to emphasize that the somewhat larger result for N^{2}LO $(550)^a$ is mainly due to the P-wave contributions. The alternative fit $(550)^b$ considered in the discussion of the $\Sigma^+ p$ cross section in Sect. 3.1, where only the P-waves were readjusted, yields $U_\Lambda = -35.9$ MeV.

By contrast, U_Σ is definitely less repulsive than what was found for NLO13 and NLO19 and also below the range of 10–50 MeV advocated in Ref. [92]. A detailed comparison reveals that the more strongly repulsive U_Σ of NLO13 and NLO19 is primarily due to the $^3S_1$ interaction in the $I = 3/2$ channel which is more repulsive at large momenta for those potentials. However, the latter feature is precisely the reason why for NLO19 the scattering results are in conflict with the J-PARC data on $\Sigma^+ p$ (cf. Fig. 1), as we have discussed in Sect. 3.1. Specifically, the artificial rise of the cross section at large momenta is a direct result of the increasingly negative values for the $^3S_1$ phase shift (Fig. 3). The same conflicting situation occurs for NLO13 and our LO interactions. Indeed, as far as we can see, also phenomenological YN potentials that predict a more strongly repulsive U_Σ, like those of Fujiwara et al. [95] based on the constituent-quark model, overestimate the $\Sigma^+ p$ cross section at large momenta, see Fig. 24 in [9].

At the moment, it remains unclear to us whether one can reconcile the constraints provided by the J-PARC data for the $\Sigma^+ p$ interaction with the request for a strongly repulsive U_Σ. Clearly, with regard to the Σ single-particle potential,

the situation could be more complicated because of the overall spin-isospin structure of the ΣN interaction where some of the relevant S-waves are attractive and others repulsive so that there are possible cancellations in the evaluation of U_Σ. That being said, and may be more importantly, one should keep in mind that the Λ single-particle potential follows from the rich spectrum of bound Λ hypernuclei and can be considered as well established. Evidence for the Σ single-particle potential comes only from the analysis of level shifts and widths of Σ^- atoms and from measurements of inclusive (π^-, K^+) spectra related to Σ^--formation in heavy nuclei [92]. It is worth mentioning that a conflicting situation has been likewise observed for the Ξ single-particle potential. Also in that case the results from Brueckner calculations, using YN interactions either constrained by available data [41] or from lattice QCD simulations [96] differ noticeably from phenomenological results deduced again mainly from atomic states and inclusive (K^-, K^+) spectra [92,97].

3.6 Uncertainty estimate

Since the range and the strength of the YN interaction is comparable to that in the NN system, considering the approximate validity of SU(3) flavor symmetry, we expect overall a very similar convergence pattern with increasing order in the chiral expansion as that found in the NN studies in Refs. [31,45]. Anyway, to corroborate this expectation, we adopt here the tools proposed in Ref. [45] for an uncertainty estimate and present some selected results below. For simplicity reasons, we focus on the elastic channels, namely Λp and $\Sigma^+ p$. One can see from the NN results [31] that S- and, in general, also P-waves are already well described at the N^{2}LO level, say for laboratory energies up to 150 MeV. The situation is different for D- and higher partial waves because, in this case, contact terms appear only at N^{3}LO or even higher order.

The concrete expression used to calculate an uncertainty $\Delta X^{\text{N}^2\text{LO}}(k)$ to the N^{2}LO prediction $X^{\text{N}^2\text{LO}}(k)$ of a given observable $X(k)$ is [45]

$$\Delta X^{\text{N}^2\text{LO}}(k) = \max \left(Q^4 \times \left| X^{\text{LO}}(k) \right|, \right.$$
$$Q^2 \times \left| X^{\text{LO}}(k) - X^{\text{NLO}}(k) \right|,$$
$$\left. Q \times \left| X^{\text{NLO}}(k) - X^{\text{N}^2\text{LO}}(k) \right| \right), \qquad (20)$$

where the expansion parameter Q is defined by

$$Q = \max \left(\frac{k}{\Lambda_b}, \frac{M_\pi}{\Lambda_b} \right), \qquad (21)$$

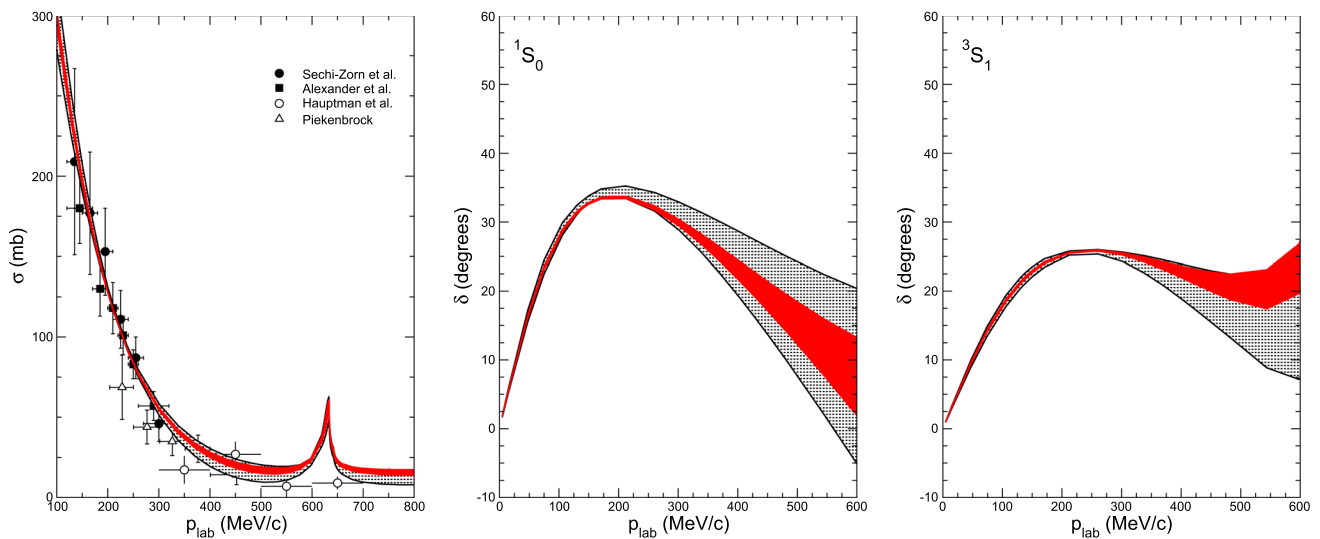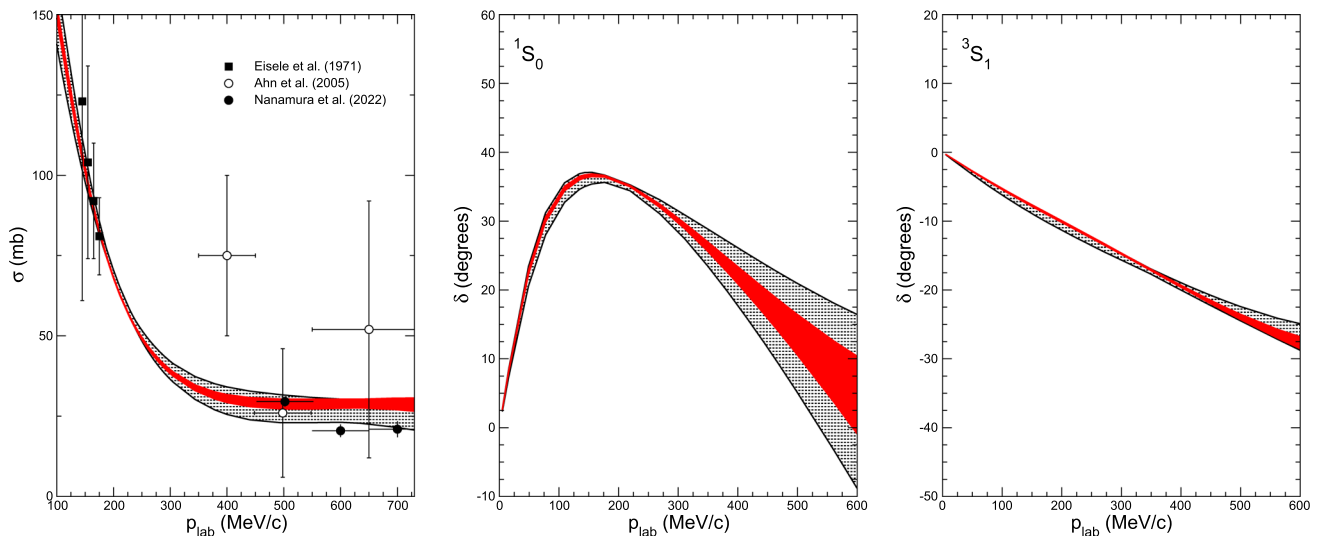with k the on-shell center-of-mass momentum corresponding to the considered laboratory energy/momentum, and Λ_b

Fig. 10 Uncertainty estimate for the YN interaction in the Λp channel, employing the method suggested in Ref. [45]. As basis the LO (700), and the NLO (550) and N^{2}LO (550) results are used. The grey (light) band corresponds to ΔX^{NLO}, the red (dark) band to $\Delta X^{\text{N}^2\text{LO}}$

Fig. 11 Uncertainty estimate for the YN interaction in the $\Sigma^+ p$ channel, employing the method suggested in Ref. [45]. Same description of the curves as in Fig. 10

the breakdown scale of the chiral EFT expansion. For the latter, we take over the value established in Ref. [45], i.e. $\Lambda_b \sim 600$ MeV. Analogous definitions are used for calculating the uncertainty up to NLO. Note that the quantity $X(k)$ represents not only a "true" observable such as a cross section or an analyzing power, but also a phase shift.

In Figs. 10 and 11, we show our uncertainty estimates for the cross sections and the S-wave phase shifts for Λp and $\Sigma^+ p$ following the procedure proposed in Ref. [45]. Certainly, for addressing the question of convergence thoroughly, orders beyond N^{2}LO are needed. Higher orders are also required to avoid that accidentally close-by results lead to an underestimation of the uncertainty. For the YN interac-

tion, any uncertainty estimate is difficult since the data are not sufficient to unambiguously determine all LECs. For example, recall that the strength of the ΛN interaction in the $^1S_0$ partial wave was fixed "by hand" and not based on actual Λp scattering data. For this reason, there is definitely some bias in the quantification of the uncertainty of phase shifts in individual partial waves. Nonetheless, we want to emphasize that the estimated uncertainty appears sensible and also plausible. In particular, it encases the variations due to the regulator dependence and, thus, is consistent with the expectation that cutoff variations provide a lower bound for the theoretical uncertainty [45]. For details of the method and a thorough discussion of the underlying concept, we refer the reader to

[98]. We should add that in case of the chiral NN interaction more sophisticated tools like a Bayesian approach [99] have been applied, too.

4 Summary and outlook

In the present work, we have established a hyperon–nucleon potential for the strangeness $S = -1$ sector (ΛN, ΣN) up to next-to-next-to-leading order in the chiral expansion. SU(3) flavor symmetry is imposed for constructing the interaction, however, the explicit SU(3) symmetry breaking by the physical masses of the pseudoscalar mesons (π, K, η) and in the leading-order contact terms is taken into account. A novel regularization scheme, the so-called semilocal momentum-space regularization, has been employed which has been already successfully applied in studies of the nucleon–nucleon interaction within chiral effective field theory up to high orders [31].

An excellent description of the low-energy Λp, $\Sigma^- p$ and $\Sigma^+ p$ scattering cross sections could be achieved with a χ^2 of 15–16 for the commonly considered 36 data points [38]. At low energies, the results are also very close to those of our earlier YN interactions NLO13 [38] and NLO19 [39], that are based on a different regularization scheme. New measurements of angular distributions for the ΣN channels from J-PARC [7–9] have been analyzed in an attempt to determine the strength of the contact interactions in the P-waves. Although those data can be fairly well described, considering the experimental uncertainties and the fact that the pertinent momenta $p_{\text{lab}} \gtrsim 450$ MeV are close to the limit of applicability of the N^{2}LO interaction, they are not included in the total χ^2.

Separation energies for the hypertriton have been presented. These are not "true" predictions of the theory, because we required the $^3_\Lambda$H to be bound as additional constraint to fix the spin dependence of the ΛN interaction. Anyway, the obtained values of 120–170 keV are well within the range of the presently existing experimental evidence [14,15,86,91]. Compared to NLO13 and NLO19, the new interaction seems to be more attractive. This also shows up in the results for $^4_\Lambda$He which are closer to the experimental values. A simple uncertainty estimate for the chiral expansion [45], performed for a selected set of YN observables, exhibits a similar pattern as has been found for the NN interaction. Certainly, at the level of N^{2}LO one can not expect to see fully converged results, in contrast to the NN sector where the calculation have progressed up to N^{4}LO (and beyond) [31].

As a next step, one should explore the YN potential in calculations of light Λ-hypernuclei within, e.g., the no-core shell model (feasible up to $A \approx 10$). Of course, for that chiral (ΛNN, ΣNN) three-body forces should be included, which arise at N^{2}LO in the chiral expansion [43]. Moreover, a pos-

sible charge-symmetry breaking in the Λp and Λn interactions should be introduced. Such a CSB component has been found to be essential for understanding the level splittings in the $^4_\Lambda$H-$^4_\Lambda$He mirror nuclei [89,90]. For example, an earlier study by us, based on the NLO13 and NLO19 interactions, suggests that $\Delta a_s = a_s^{\Lambda p} - a_s^{\Lambda n} \approx 0.62 \pm 0.08$ fm for $^1 S_0$ and $\Delta a_t \approx -0.10 \pm 0.02$ fm for $^3 S_1$ [89]. Clearly, the reproduction of the large CSB effect in the $^1 S_0$ partial wave requires a noticeable modification of the present ΛN interaction. In any case, one has to keep in mind that the actual CSB splittings for $^4_\Lambda$H-$^4_\Lambda$He are not yet that well settled experimentally, cf. Refs. [16,91,100]. Finally, a more elaborate effort to determine the strength of the contact terms in the P-waves should be done in the future when Λp angular distributions from the J-PARC E86 experiment have become available [42].

Data Availability Statement This manuscript has no associated data or the data will not be deposited. [Authors' comment: All data are contained in the figures and tables.]

Appendix A: Semilocal momentum-space baryon-baryon potential at NLO and N^{2}LO

In order to implement the local cutoff in the two-meson contributions we follow Ref. [31] and write the corresponding
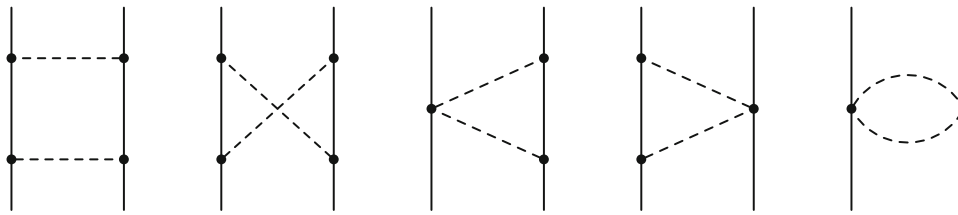
Fig. 12 Relevant diagrams at next-to-leading order. Solid and dashed lines denote octet baryons and pseudoscalar mesons, respectively. From left to right: planar box, crossed box, left triangle, right triangle, football diagram. Note that from the planar box, only the irreducible part contributes to the potential

potentials in terms of their spectral representation:

$$
V(q) = \frac{2}{\pi} \int_{2M_P}^{\infty} \mu \, d\mu \frac{\rho(\mu)}{\mu^2 + q^2} \, ,
$$
$$
\rho(\mu) = \mathrm{Im} V(q = 0^+ - \mathrm{i}\,\mu) \tag{A.1}
$$

with q the momentum transfer $q = |\mathbf{p}' - \mathbf{p}|$ and M_P the mass of the exchanged meson. The regularized potential is then given by

$$
V(q) = e^{-\frac{q^2}{2\Lambda^2}} \frac{2}{\pi} \int_{2M_P}^{\infty} \mu \, d\mu \frac{\rho(\mu)}{\mu^2 + q^2} \, e^{-\frac{\mu^2}{2\Lambda^2}} \, . \tag{A.2}
$$

Appendix A.1: Contributions at NLO

Diagrams representing the contributions at NLO (chiral order $\nu = 2$) are shown in Fig. 12. At NLO one obtains a central potential (V_C), a spin-spin potential (V_S) and a tensor-type potential (V_T) [38], so that $V^{(2)} = V_C^{(2)} + \boldsymbol{\sigma}_1 \cdot \boldsymbol{\sigma}_2 \, V_S^{(2)} + \boldsymbol{\sigma}_1 \cdot \mathbf{q} \, \boldsymbol{\sigma}_2 \cdot \mathbf{q} \, V_T^{(2)}$. We provide here explicit expressions of the irreducible potentials for two-pion exchange [31,101]. Clearly, those formulae are also valid for $\eta\eta$ and/or KK ($K\bar{K}$) exchange. General expressions of the spectral functions for non-identical meson masses are given in Appendix B below.

$$
V_{C,S}^{(2)}(q) = \frac{2q^4}{\pi} \int_{2M_\pi}^{\infty} d\mu \frac{\rho_{C,S}(\mu)}{\mu^3 (\mu^2 + q^2)},
$$
$$
V_T^{(2)}(q) = -\frac{2q^2}{\pi} \int_{2M_\pi}^{\infty} d\mu \frac{\rho_T(\mu)}{\mu (\mu^2 + q^2)}. \tag{A.3}
$$

The contributions (spectral functions) of the individual diagrams are:
Planar box (pb)

$$
\rho_C^{pb}(\mu) = -\frac{N}{3072\pi f_0^4 \sqrt{\mu^2 - 4M_\pi^2}\,\mu}
$$
$$
\times (-23\mu^4 + 112\mu^2 M_\pi^2 - 128 M_\pi^4), \tag{A.4}
$$
$$
\rho_T^{pb}(\mu) = \frac{\rho_S^{pb}(\mu)}{\mu^2} = \frac{N\sqrt{\mu^2 - 4M_\pi^2}}{256\pi f_0^4 \,\mu}. \tag{A.5}
$$

Crossed box (xb)

$$
\rho_C^{xb}(\mu) = -\rho_C^{pb}(\mu),
$$

$$
\rho_S^{xb}(\mu) = \rho_S^{pb}(\mu),
$$
$$
\rho_T^{xb}(\mu) = \rho_T^{pb}(\mu). \tag{A.6}
$$

Triangle diagrams (tr)

$$
\rho_C(\mu) = -\frac{N\sqrt{\mu^2 - 4M_\pi^2}}{3072\pi f_0^4 \,\mu} (5\mu^2 - 8M_\pi^2). \tag{A.7}
$$

Football diagram (fb)

$$
\rho_C(\mu) = -\frac{N(\mu^2 - 4M_\pi^2)^{3/2}}{6144\pi f_0^4 \,\mu}. \tag{A.8}
$$

The quantities N are an appropriate product of coupling constants and isospin factors:

$$
\begin{aligned}
N^{pb,xb} &= f_{B_1 B_{il} M_1} f_{B_{il} B_3 M_2} \\
&\quad \times f_{B_2 B_{ir} M_2} f_{B_{ir} B_4 M_1} (2f_0)^4 \, \mathcal{I}_{B_1 B_2 \to B_3 B_4} \\
N^{tr} &= f_{B_1 B_i M_1} f_{B_i B_3 M_2} (2f_0)^2 \, \mathcal{I}_{B_1 B_2 \to B_3 B_4} \\
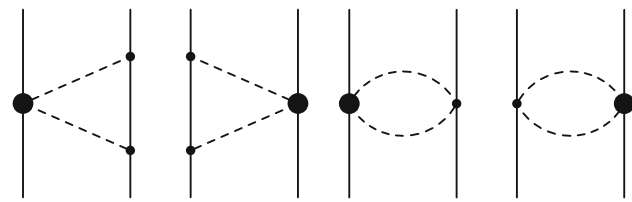N^{fb} &= \mathcal{I}_{B_1 B_2 \to B_3 B_4}.
\end{aligned} \tag{A.9}
$$

The isospin factors are summarized in Table 7 whereas the coupling constants are specified in Eqs. (4). B_{il} and B_{ir} denote the (left and right) baryons in the intermediate state. Note that the relations (A.6) concern only the μ dependence, but not the factors N^{pb} and N^{xb}! In case of the NN system the expressions for the spectral functions (and the potential) can be reduced to those given in Ref. [31] by simply representing the pertinent isospin coefficients in Table 7 in operator form: $-2\,\boldsymbol{\tau}_1 \cdot \boldsymbol{\tau}_2 + 3$ for the planar box, $2\,\boldsymbol{\tau}_1 \cdot \boldsymbol{\tau}_2 + 3$ for the crossed box, $-4\,\boldsymbol{\tau}_1 \cdot \boldsymbol{\tau}_2$ for the triangle diagrams, and $8\,\boldsymbol{\tau}_1 \cdot \boldsymbol{\tau}_2$ for the football diagram. Then, since $V_C^{xb} = -V_C^{pb}$, see Eq. (A.6), the central component of the spectral function (potential) is proportional to $\boldsymbol{\tau}_1 \cdot \boldsymbol{\tau}_2$ (denoted by η_C and W_C, respectively, in Ref. [31]), while for the spin- and tensor components the contributions from planar and crossed box add up and the isospin dependence drops out ($\rho_{S,T}$ and $V_{S,T}$ in Ref. [31]).

Appendix A.2: Contributions at N²LO

Diagrams that arise at N²LO ($\nu = 3$) are shown in Fig. 13. It should be noted, however, that only the triangle diagrams contribute. There is no contribution from the football diagram because of parity conservation. The potential consists

Table 7 Isospin factors $\mathcal{I}$ for the NLO diagrams. The baryons in the intermediate state of the planar box, crossed box, and the triangle diagrams are indicated to the left of the factors

Transition (isospin)	Planar Box		Crossed Box		Triangle Left		Triangle Right		Football Diagram
$NN \to NN$									
$(I = 0)$	NN	9	NN	-3	N	12	N	12	-24
$(I = 1)$	NN	1	NN	5	N	-4	N	-4	8
$\Sigma N \to \Sigma N$									
$(I = 1/2)$	ΣN	4	ΣN	0	N	16	Σ	4	-32
	ΛN	3	ΛN	-1			Λ	4	
$(I = 3/2)$	ΣN	1	ΣN	3	N	-8	Σ	-2	16
	ΛN	0	ΛN	2			Λ	-2	
$\Lambda N \to \Sigma N$									
$(I = 1/2)$	ΣN	$2\sqrt{3}$	ΣN	$-2\sqrt{3}$	N	0	Σ	$4\sqrt{3}$	0
$\Lambda N \to \Lambda N$									
$(I = 1/2)$	ΣN	3	ΣN	3	N	0	Σ	0	0

Fig. 13 Relevant diagrams at next-to-next-to-leading order. Solid and dashed lines denote octet baryons and pseudoscalar mesons, respectively. Triangle (left) and football (right) diagram

again of central, spin-spin, and tensor components, $V_{C,S,T}^{(3)}$, and those components can be evaluated from representations analogous to Eq. (A.3). The spectral functions in question are given by [101]

$$\rho_C(\mu) = \frac{N_1}{512\mu f_0^4}(\mu^2 - 2M_\pi^2) + \frac{N_2}{256\mu f_0^4}(\mu^2 - 2M_\pi^2)^2,$$
(A.10)

$$\rho_T(\mu) = \frac{\rho_S(\mu)}{\mu^2} = -\frac{N_3}{512\mu f_0^4}(\mu^2 - 4M_\pi^2).$$
(A.11)

The coefficients N_i ($i = 1, 2, 3$) are combinations of the coupling constants at the involved BBM vertices and of elements of the sub-leading ($\mathcal{O}(q^2)$) meson-baryon Lagrangian [102,103], in particular of the meson-baryon LECs b_D, b_F, b_0, b_1-b_4, and d_1-d_3, see Sect. IV in Ref. [43] for details and/or Sect. 4.3 in [46]. The concrete relations are as follows: for NN

$$N_1 = 96\, c_1\, g_A^2\, M_\pi^2,$$
$$N_2 = 12\, c_3\, g_A^2,$$
$$N_3 = -4\, c_4\, g_A^2\, \boldsymbol{\tau}_1 \cdot \boldsymbol{\tau}_2,$$
(A.12)

with $c_1 = (2b_0 + b_D + b_F)/2$, $c_3 = b_1 + b_2 + b_3 + 2b_4$, $c_4 = 4(d_1 + d_2)$ [104], where the c_i are the conventional LECs used in the nucleonic sector.

for ΣN

$$N_1 = \Big[48\, c_1^\Sigma\, g_A^2 + 32\, c_1\, (2\alpha g_A)^2$$
$$\qquad + 16\, c_1\, \frac{4}{3}((1-\alpha)g_A)^2 \Big] M_\pi^2,$$

$$N_2 = 4c_3^\Sigma\, g_A^2 + 4c_3\, (2\alpha g_A)^2 + 2c_3\, \frac{4}{3}((1-\alpha)g_A)^2,$$

$$N_3 = -\left(4d^\Sigma\, g_A^2 + c_4\, (2\alpha g_A)^2 + c_4\, \frac{4}{3}((1-\alpha)g_A)^2 \right) \boldsymbol{T}_1 \cdot \boldsymbol{\tau}_2,$$
(A.13)

with $c_1^\Sigma = b_0 + b_D$, $c_3^\Sigma = 4b_1 + 2b_2 + 3b_4$, and $d^\Sigma = 4d_2 + d_3$ and $\langle \boldsymbol{T}_1 \cdot \boldsymbol{\tau}_2 \rangle = -2, 1$ for isospin $I = 1/2, 3/2$.

for ΛN

$$N_1 = \Big[16\, c_1^\Lambda\, g_A^2 + 48\, c_1\, \frac{4}{3}((1-\alpha)g_A)^2 \Big] M_\pi^2,$$

$$N_2 = 4\, c_3^\Lambda\, g_A^2 + 6\, c_3\, \frac{4}{3}((1-\alpha)g_A)^2,$$

$$N_3 = 0,$$
(A.14)

with $c_1^\Lambda = 3b_0 + b_D$, $c_3^\Lambda = 2b_2 + 3b_4$.

for $\Lambda N \to \Sigma N$

$$N_1 = 0,$$
$$N_2 = 0,$$
$$N_3 = 16d_1\, g_A^2 + 2\sqrt{3}\, c_4\, \frac{4}{\sqrt{3}}\alpha(1-\alpha)g_A^2.$$
(A.15)

Note that in Eqs. (A.13–A.15) we have re-expressed the $\Sigma\Sigma\pi$ and $\Sigma\Lambda\pi$ coupling constants in terms of the SU(3) relations given in Eq. (4), i.e. $f_{\Sigma\Sigma\pi} = 2\alpha f_{NN\pi}$ and $f_{\Sigma\Lambda\pi} = (2/\sqrt{3})(1-\alpha)f_{NN\pi}$ with $f_{NN\pi} = g_A/(2f_\pi)$.

In our calculation we take the πN LECs, i.e. c_1-c_4, from Refs. [105,106], obtained from matching the chiral expansion of the pion-nucleon scattering amplitude to the solution

of the Roy-Steiner equations. Specifically we use the values employed in the SMS NN potential up to N^{2}LO. Fixing the values for the other LECs, without direct experimental evidence which can be used as constraint, is, however, difficult, and to some extent arbitrary. Here we try to find the best possible set instead of insisting on an intrinsically consistent selection. Since theoretical studies of the baryon masses yield, in general, b_1,...,b_4 values that imply a c_3 very far away from the results obtained from πN scattering we consider the values from decuplet saturation as the most realistic choice. Accordingly, we take the values for the b's and d's (i.e. b_1-b_4, d_1-d_3) for the $\pi \Sigma$ and $\pi \Lambda$ vertices from Ref. [107]. Since b_D, b_F, b_0 are zero in this case, we use here values from Ref. [108], fixed in a study of the baryon mass splittings and the πN sigma term. Anyway exploratory calculations indicated that the YN results are fairly insensitive to the specific values adopted for the LECs b_D, b_F, b_0. The actual values used are (all in units of GeV^{-1}): $c_1 = -0.74$, $c_3 = -3.61$, $c_4 = -2.44$ [105,106], $b_D = 0.066$, $b_F = -2.13$, $b_0 = -0.517$ [108], $b_1 = 0.59$, $b_2 = 0.76$, $b_3 = -1.01$, $b_4 = -1.51$, $d_1 = 0.25$, $d_2 = 0.08$, $d_3 = -0.50$ [107].

Appendix A.3: Subtractions in the spectral integrals

As in case of the LO term and following the procedure in the NN interaction [31] we perform subtractions according to Eqs. (42) and (44) of that reference in the spectral integrals for the NLO and N^{2}LO potentials so that the final form of those contributions read

$$V_C^{(2,3)}(q) = e^{-\frac{q^2}{2\Lambda^2}} \frac{2}{\pi} \int_{2M_\pi}^\infty \frac{d\mu}{\mu^3} \rho_C^{(2,3)}(\mu)$$
$$\times \left(\frac{q^4}{\mu^2 + q^2} + C_{C,1}^2(\mu) + C_{C,2}^2(\mu) q^2 \right) e^{-\frac{\mu^2}{2\Lambda^2}},$$

$$V_S^{(2,3)}(q) = e^{-\frac{q^2}{2\Lambda^2}} \frac{2}{\pi} \int_{2M_\pi}^\infty \frac{d\mu}{\mu^3} \rho_S^{(2,3)}(\mu)$$
$$\times \left(\frac{q^4}{q^2 + \mu^2} + C_{S,1}^2(\mu) + C_{S,2}^2(\mu) q^2 \right) e^{-\frac{\mu^2}{2\Lambda^2}},$$

$$V_T^{(2,3)}(q) = -e^{-\frac{q^2}{2\Lambda^2}} \frac{2}{\pi} \int_{2M_\pi}^\infty \frac{d\mu}{\mu^3} \rho_S^{(2,3)}(\mu)$$
$$\times \left(\frac{q^2}{\mu^2 + q^2} + C_T^1(\mu) \right) e^{-\frac{\mu^2}{2\Lambda^2}}, \qquad \text{(A.16)}$$

The functions $C_i^2(\mu)$ and $C_T^1(\mu)$ appearing in the (single- and double-)subtracted spectral integrals have the form [31]:

$$C_{C,1}^2(\mu) = \left[2\Lambda\mu^2 \left(2\Lambda^4 - 4\Lambda^2\mu^2 - \mu^4 \right) \right.$$
$$\left. + \sqrt{2\pi}\mu^5 e^{\frac{\mu^2}{2\Lambda^2}} \left(5\Lambda^2 + \mu^2 \right) \text{erfc}\left(\frac{\mu}{\sqrt{2}\Lambda} \right) \right]$$
$$/(4\Lambda^5),$$

$$C_{C,2}^2(\mu) = -\left[2\Lambda \left(6\Lambda^6 - 2\Lambda^2\mu^4 - \mu^6 \right) \right.$$

$$\left. + \sqrt{2\pi}\mu^5 e^{\frac{\mu^2}{2\Lambda^2}} \left(3\Lambda^2 + \mu^2 \right) \text{erfc}\left(\frac{\mu}{\sqrt{2}\Lambda} \right) \right]$$
$$/(12\Lambda^7),$$

$$C_{S,1}^2(\mu) = \left[2\Lambda\mu^2 \left(2\Lambda^4 - 4\Lambda^2\mu^2 - \mu^4 \right) \right.$$
$$\left. + \sqrt{2\pi}\mu^5 e^{\frac{\mu^2}{2\Lambda^2}} \left(5\Lambda^2 + \mu^2 \right) \text{erfc}\left(\frac{\mu}{\sqrt{2}\Lambda} \right) \right]$$
$$/(6\Lambda^5),$$

$$C_{S,2}^2(\mu) = -\left[2\Lambda \left(15\Lambda^6 - \Lambda^4\mu^2 - 3\Lambda^2\mu^4 - 2\mu^6 \right) \right.$$
$$\left. + \sqrt{2\pi}\mu^5 e^{\frac{\mu^2}{2\Lambda^2}} \left(5\Lambda^2 + 2\mu^2 \right) \text{erfc}\left(\frac{\mu}{\sqrt{2}\Lambda} \right) \right]$$
$$/(30\Lambda^7),$$

$$C_T^1(\mu) = -\left[2\Lambda \left(15\Lambda^6 - 3\Lambda^4\mu^2 + \Lambda^2\mu^4 - \mu^6 \right) \right.$$
$$\left. + \sqrt{2\pi}\mu^7 e^{\frac{\mu^2}{2\Lambda^2}} \text{erfc}\left(\frac{\mu}{\sqrt{2}\Lambda} \right) \right]$$
$$/(30\Lambda^7). \qquad \text{(A.17)}$$

Appendix B: Spectral functions for unequal meson masses

For completeness we provide here expressions for the spectral functions when the masses of the mesons are different. Those can be used to evaluate the contributions from exchanges of πK, ηK, etc., which arise formally in SU(3) chiral EFT at NLO and N^{2}LO. However, as already emphasized in the main text, given the present choice of the cutoff in the local regulator of $\Lambda = 500$–600 MeV, those contributions are strongly suppressed and, therefore, omitted in the present study. Denoting the meson masses by M_1 and M_2 the spectral functions are as follows:
for NLO

$$\rho_C^{pb}(\mu) = \frac{-\dfrac{N}{3072\pi f_0^4}}{\sqrt{\left[\mu^2 - (M_1 + M_2)^2\right]\left[\mu^2 - (M_1 - M_2)^2\right]}}$$
$$\times \left[-23\mu^4 + \frac{(M_1^2 - M_2^2)^4}{\mu^4} + 56\mu^2(M_1^2 + M_2^2) \right.$$
$$+ 8\frac{(M_1^2 + M_2^2)(M_1^2 - M_2^2)^2}{\mu^2}$$
$$\left. - 2(21M_1^4 + 22M_1^2 M_2^2 + 21M_2^4) \right] \qquad \text{(A.18)}$$

$$\rho_T^{pb}(\mu) = \frac{\rho_S^{pb}(\mu)}{\mu^2}$$
$$= \frac{N\sqrt{\left[\mu^2 - (M_1 + M_2)^2\right]\left[\mu^2 - (M_1 - M_2)^2\right]}}{256\pi\mu^2 f_0^4} \qquad \text{(A.19)}$$

For crossed-box diagrams the relations given in Eq. (A.6) apply.

$$\rho_C^{tr}(\mu) = -\frac{N\sqrt{[\mu^2-(M_1+M_2)^2][\mu^2-(M_1-M_2)^2]}}{3072\pi\mu^4 f_0^4}$$
$$\times \left[5\mu^4 - 4\mu^2(M_1^2+M_2^2) - (M_1^2-M_2^2)^2\right] \tag{A.20}$$

$$\rho_C^{fb}(\mu) = \frac{N[\mu^2-(M_1+M_2)^2]^{\frac{3}{2}}[\mu^2-(M_1-M_2)^2]^{\frac{3}{2}}}{6144\pi\mu^4 f_0^4} \tag{A.21}$$

for N²LO

$$\rho_C^{tr}(\mu) = \frac{N_1}{512\mu f_0^4}(\mu^2 - M_1^2 - M_2^2)$$
$$+ \frac{N_2}{256\mu f_0^4}(\mu^2 - M_1^2 - M_2^2)^2 \tag{A.22}$$

$$\rho_T^{tr}(\mu) = \frac{\rho_S^{tr}(\mu)}{\mu^2}$$

$$= -\frac{N_3}{512\mu^3 f_0^4}\left[\mu^2 - (M_1+M_2)^2\right]$$
$$\times \left[\mu^2 - (M_1-M_2)^2\right] \tag{A.23}$$

Appendix C: Tables with LECs

The YN LECs employed in the present study are summarized in Tables 8 and 9. With those LECs the contribution of the contact terms to the potentials in the various YN channels can be calculated, based on Eqs. (8) to (17). With regard to the P-waves SU(3) symmetry is preserved so that the potentials follow from the appropriate SU(3) combination as specified in Table 2. In case of the $^1S_0$ and $^3S_1$-$^3D_1$ partial waves, leading-order SU(3) breaking terms have been considered in the fitting procedure, in line with the power counting [50]. Here, we list the LECs in the isospin basis for the ΛN and ΣN channels and the $\Lambda N \leftrightarrow \Sigma N$ transition (Table 8). Since for the $^3S_1$-$^3D_1$ partial wave SU(3) symmetry implies that $V_{\Lambda N \to \Lambda N} = V_{\Sigma N \to \Sigma N (I=1/2)} = (C^{8_a} + C^{10^*})/2$, cf. Table 2, one can directly read off the amount of symmetry

Table 8 The YN contact terms for the $^1S_0$ and $^3S_1$–$^3D_1$ partial waves for various cutoffs. The values of the $\tilde{C}$'s are in 10^4 GeV^{-2} the ones of the C's in 10^4 GeV^{-4}; the values of Λ in MeV

		SMS NLO			SMS N²LO		
Λ		500	550	600	500	550	600
$\Lambda N \to \Lambda N$	$\tilde{C}_{^1S_0}$	−0.02935	−0.00329	0.14237	0.00494	0.07219	0.08299
	$C_{^1S_0}$	0.63280	0.61297	0.79287	0.26538	0.37189	0.09995
$\Lambda N \to \Sigma N$	$\tilde{C}_{^1S_0}$	−0.03286	−0.03023	−0.11525	−0.02415	−0.06843	−0.07698
	$C_{^1S_0}$	−0.29427	−0.26766	−0.33429	−0.11513	−0.17396	−0.02095
$\Sigma N \to \Sigma N$ (1/2)	$\tilde{C}_{^1S_0}$	0.11221	0.12683	0.14184	0.09486	0.17822	0.29980
	$C_{^1S_0}$	−0.15191	−0.10078	−0.09857	−0.04162	−0.09201	0.04409
$\Sigma N \to \Sigma N$ (3/2)	$\tilde{C}_{^1S_0}$	−0.01620	0.02679	0.17627	0.00309	0.06730	0.07276
	$C_{^1S_0}$	0.73089	0.70219	0.90430	0.30375	0.42988	0.10693
$\Lambda N \to \Lambda N$	$\tilde{C}_{^3S_1}$	0.09667	0.10212	0.14003	0.16132	0.18609	0.21782
	$C_{^3S_1}$	0.72758	0.56012	0.54597	0.39114	0.34187	0.16242
$\Lambda N \to \Sigma N$	$\tilde{C}_{^3S_1}$	0.15685	0.18472	0.19931	0.17541	0.16851	0.18866
	$C_{^3S_1}$	0.72892	0.27346	−0.05722	0.58414	0.49310	0.15400
$\Sigma N \to \Sigma N$ (1/2)	$\tilde{C}_{^3S_1}$	0.09667	0.10212	0.14003	0.18681	0.18877	0.21267
	$C_{^3S_1}$	0.72758	0.56012	0.54597	0.39114	0.34187	0.16242
$\Sigma N \to \Sigma N$ (3/2)	$\tilde{C}_{^3S_1}$	0.05032	0.06086	0.06355	0.15319	0.11209	0.13002
	$C_{^3S_1}$	0.08219	0.08044	0.03758	0.40259	−0.06077	−0.10236
$\Lambda N \to \Lambda N$	$C_{^3SD_1}$	0.08863	0.09803	0.08863	0.34868	0.13053	0.12134
$\Lambda N \to \Sigma N$	$C_{^3SD_1}$	0.31634	0.32118	0.31634	0.52449	0.32367	0.34512
$\Sigma N \to \Sigma N$ (1/2)	$C_{^3SD_1}$	0.08863	0.09803	0.08863	0.34868	0.13053	0.12134
$\Sigma N \to \Sigma N$ (3/2)	$C_{^3SD_1}$	0.20000	0.24793	0.24793	0.21463	0.21463	0.18000

Table 9 The YN contact terms for the P-waves for various cutoffs. The values of the LECs are in 10^4 GeV^{-4}; the values of Λ in MeV. The superscripts a and b denote the two variants introduced in Sect. 3.1

Λ	SMS NLO			SMS N^{2}LO			
	500	550	600	500	550^a	550^b	600
$C^{27}_{^3P_0}$	0.17477	0.22196	0.26500	0.44332	0.45000	0.62505	0.61226
$C^{8_s}_{^3P_0}$	1.65980	2.75900	2.06930	2.39600	0.82218	1.60990	2.42460
$C^{10^*}_{^1P_1}$	2.41220	1.62550	0.82692	2.41640	1.55430	1.73930	3.14090
$C^{10}_{^1P_1}$	0.00000	0.00000	0.00000	0.32168	0.20699	−0.09449	0.03500
$C^{8_a}_{^1P_1}$	0.06119	−0.10810	−0.14370	0.14853	0.19339	0.20985	0.32815
$C^{27}_{^3P_1}$	0.22993	0.19541	0.18500	0.32000	0.48651	0.65850	0.58177
$C^{8_s}_{^3P_1}$	0.39891	0.07447	0.10685	0.49239	0.51190	0.52342	0.79248
$C^{27}_{^3P_2}$	−0.29185	−0.25446	−0.22000	−0.08937	−0.10000	−0.01692	−0.01802
$C^{8_s}_{^3P_2}$	1.06570	−0.06844	−0.20845	2.96720	3.30420	3.32790	2.96270

breaking in the contribution of the contact potential from the values in Table 8. In general, it is small or even zero.

References

1. D. Chatterjee, I. Vidaña, Do hyperons exist in the interior of neutron stars? Eur. Phys. J. A **52**(2), 29 (2016). https://doi.org/10.1140/epja/i2016-16029-x. arXiv:1510.06306

2. J. Schaffner-Bielich, Compact Star Physics. Cambridge University Press (2020). https://doi.org/10.1017/9781316848357

3. L. Tolos, L. Fabbietti, Strangeness in nuclei and neutron stars. Prog. Part. Nucl. Phys. **112**, 103770 (2020). https://doi.org/10.1016/j.ppnp.2020.103770. arXiv:2002.09223

4. W. Weise, Equation of state and strangeness in neutron stars—role of hyperon-nuclear three-body forces. EPJ Web Conf. **271**, 06003 (2022). https://doi.org/10.1051/epjconf/202227106003. arXiv:2208.14831

5. E. Friedman, A. Gal, Constraints from Λ hypernuclei on the ΛNN content of the Λ-nucleus potential. Phys. Lett. B **837** 137669 (2023). arXiv:2204.02264

6. J. Rowley et al., Improved Λp Elastic Scattering Cross Sections Between 0.9 and 2.0 GeV/c and Connections to the Neutron Star Equation of State. Phys. Rev. Lett. **127**(27), 272303 (2021). https://doi.org/10.1103/PhysRevLett.127.272303. arXiv:2108.03134

7. K. Miwa et al., Measurement of the differential cross sections of the $\Sigma^- p$ elastic scattering in momentum range 470 to 850 MeV/c. Phys. Rev. C **104**(4), 045204 (2021). https://doi.org/10.1103/PhysRevC.104.045204. arXiv:2104.13608

8. K. Miwa et al., Precise measurement of differential cross sections of the $\Sigma^- p \to \Lambda n$ reaction in momentum range 470–650 MeV/c. Phys. Rev. Lett. **128**(7), 072501 (2022). https://doi.org/10.1103/PhysRevLett.128.072501. arXiv:2111.14277

9. T. Nanamura, et al. Measurement of differential cross sections for $\Sigma + p$ elastic scattering in the momentum range 0.44–0.80 GeV/c. PTEP, 2022(9):093D01, 2022. arXiv:2203.08393, https://doi.org/10.1093/ptep/ptac101

10. J. Adams et al., Proton - lambda correlations in central Au+Au collisions at $\sqrt{(s_{NN})}$ = 200 GeV. Phys. Rev. C **74**, 064906 (2006). https://doi.org/10.1103/PhysRevC.74.064906. arXiv:nucl-ex/0511003

11. J. Adamczewski-Musch et al. The Λp interaction studied via femtoscopy in p + Nb reactions at $\sqrt{s_{NN}}$ = 3.18**GeV**. *Phys. Rev. C*, 94(2):025201, (2016). arXiv:1602.08880, https://doi.org/10.1103/PhysRevC.94.025201

12. S. Acharya et al., Exploring the NΛ-NΣ coupled system with high precision correlation techniques at the LHC. Phys. Lett. B **833**, 137272 (2022). https://doi.org/10.1016/j.physletb.2022.137272. arXiv:2104.04427

13. S. Acharya et al., Investigation of the p-Σ^0 interaction via femtoscopy in pp collisions. Phys. Lett. B **805**, 135419 (2020). https://doi.org/10.1016/j.physletb.2020.135419. arXiv:1910.14407

14. J. Adam et al., Measurement of the mass difference and the binding energy of the hypertriton and antihypertriton. Nature Phys. **16**(4), 409–412 (2020). https://doi.org/10.1038/s41567-020-0799-7. arXiv:1904.10520

15. ALICE, Measurement of the lifetime and Λ separation energy of $^3_\Lambda$H. (2022). arXiv:2209.07360

16. M. Abdallah et al., Measurement of $^4_\Lambda$H and $^4_\Lambda$He binding energy in Au+Au collisions at $\sqrt{s_{NN}}$ = 3 GeV. Phys. Lett. B **834**, 137449 (2022). https://doi.org/10.1016/j.physletb.2022.137449. arXiv:2207.00778

17. H. Nemura et al., Baryon interactions from lattice QCD with physical masses-strangeness $S = -1$ sector. EPJ Web Conf. **175**, 05030 (2018). https://doi.org/10.1051/epjconf/201817505030. arXiv:1711.07003

18. H. Nemura, Lambda-Nucleon and Sigma-Nucleon potentials from space-time correlation function on the lattice. PoS, LATTICE2021:272, 2022. https://doi.org/10.22323/1.396.0272. arXiv:2203.07661

19. R. Wirth, D. Gazda, P. Navrátil, A. Calci, J. Langhammer, R. Roth, Ab initio description of p-shell hypernuclei. Phys. Rev. Lett. **113**(19), 192502 (2014). https://doi.org/10.1103/PhysRevLett.113.192502. arXiv:1403.3067

20. R. Wirth, D. Gazda, P. Navrátil, R. Roth, Hypernuclear no-core shell model. Phys. Rev. C **97**(6), 064315 (2018). https://doi.org/10.1103/PhysRevC.97.064315. arXiv:1712.05694

21. R. Wirth, R. Roth, Similarity renormalization group evolution of hypernuclear Hamiltonians. Phys. Rev. C **100**(4), 044313 (2019). https://doi.org/10.1103/PhysRevC.100.044313. arXiv:1902.03324

22. H. Le, J. Haidenbauer, U.-G. Meißner, A. Nogga, Jacobi no-core shell model for p-shell hypernuclei. Eur. Phys. J. A **56**(12),

301 (2020). https://doi.org/10.1140/epja/s10050-020-00314-6. arXiv:2008.11565

23. H. Le, J. Haidenbauer, U.-G. Meißner, A. Nogga, S-shell $\Lambda\Lambda$ hypernuclei based on chiral interactions. Eur. Phys. J. A **57**(7), 217 (2021). https://doi.org/10.1140/epja/s10050-021-00522-8. arXiv:2103.08395

24. H. Le, J. Haidenbauer, U.-G. Meißner, A. Nogga, $A = 4 - 7\Xi$ hypernuclei based on interactions from chiral effective field theory. Eur. Phys. J. A **57**(12), 339 (2021). https://doi.org/10.1140/epja/s10050-021-00653-y. arXiv:2109.06648

25. Hoai Le, Johann Haidenbauer, Ulf-G. Meißner, Andreas Nogga, Ab initio calculation of charge symmetry breaking in $A = 7$ and 8 Λ-hypernuclei. Phys. Rev. C **107**, 024002 (2023). arXiv:2210.03387

26. S. Weinberg, Nuclear forces from chiral Lagrangians. Phys. Lett. B **251**, 288–292 (1990). https://doi.org/10.1016/0370-2693(90)90938-3

27. S. Weinberg, Effective chiral Lagrangians for nucleon–pion interactions and nuclear forces. Nucl. Phys. B **363**, 3–18 (1991). https://doi.org/10.1016/0550-3213(91)90231-L

28. E. Epelbaum, H.-W. Hammer, U.-G. Meißner, Modern Theory of Nuclear Forces. Rev. Mod. Phys. **81**, 1773–1825 (2009). https://doi.org/10.1103/RevModPhys.81.1773. arXiv:0811.1338

29. R. Machleidt, D.R. Entem, Chiral effective field theory and nuclear forces. Phys. Rep. **503**(1), 1–75 (2011). https://doi.org/10.1016/j.physrep.2011.02.001. arXiv:1105.2919 [nucl-th]

30. E. Epelbaum, H. Krebs, Ulf-G. Meißner, Precision nucleon-nucleon potential at fifth order in the chiral expansion. Phys. Rev. Lett. **115**(12)(2015). https://doi.org/10.1103/PhysRevLett.115.122301. arXiv:1412.4623

31. P. Reinert, H. Krebs, E. Epelbaum, Semilocal momentum-space regularized chiral two-nucleon potentials up to fifth order. Eur. Phys. J. A **54**(5), 86 (2018). https://doi.org/10.1140/epja/i2018-12516-4. arXiv:1711.08821

32. D.R. Entem, R. Machleidt, Y. Nosyk, High-quality two-nucleon potentials up to fifth order of the chiral expansion. Phys. Rev. C **96**(2), 024004 (2017). https://doi.org/10.1103/PhysRevC.96.024004. arXiv:1703.05454

33. C.L. Korpa, A.E.L. Dieperink, R.G.E. Timmermans, Hyperon nucleon scattering and hyperon masses in the nuclear medium. Phys. Rev. C **65**, 015208 (2002). https://doi.org/10.1103/PhysRevC.65.015208. arXiv:nucl-th/0109072

34. H. Polinder, J. Haidenbauer, U.-G. Meißner, Hyperon-nucleon interactions: A Chiral effective field theory approach. Nucl. Phys. A **779**, 244 (2006). https://doi.org/10.1016/j.nuclphysa.2006.09.006. arXiv:nucl-th/0605050

35. K.-W. Li, X.-L. Ren, L.-S. Geng, B. Long, Strangeness $S = -1$ hyperon-nucleon scattering in covariant chiral effective field theory. Phys. Rev. D **94**(1), 014029 (2016). https://doi.org/10.1103/PhysRevD.94.014029. arXiv:1603.07802

36. X.L. Ren, E. Epelbaum, J. Gegelia, Λ-nucleon scattering in baryon chiral perturbation theory. Phys. Rev. C **101**(3), 034001 (2020). https://doi.org/10.1103/PhysRevC.101.034001. arXiv:1911.05616

37. J. Song, Z.-W. Liu, K.-W. Li, L.-S. Geng, Test of the hyperon–nucleon interaction within leading order covariant chiral effective field theory. Phys. Rev. C **105**(3), 035203 (2022). https://doi.org/10.1103/PhysRevC.105.035203. arXiv:2107.04742

38. J. Haidenbauer, S. Petschauer, N. Kaiser, U.-G. Meißner, A. Nogga, W. Weise, Hyperon–nucleon interaction at next-to-leading order in chiral effective field theory. Nucl. Phys. A **915**, 24–58 (2013). https://doi.org/10.1016/j.nuclphysa.2013.06.008. arXiv:1304.5339

39. J. Haidenbauer, U.-G. Meißner, A. Nogga, Hyperon–nucleon interaction within chiral effective field theory revisited. Eur.

40. Phys. J. A **56**(3), 91 (2020). https://doi.org/10.1140/epja/s10050-020-00100-4. arXiv:1906.11681

40. J. Haidenbauer, U.-G. Meißner, S. Petschauer, Strangeness S = -2 baryon-baryon interaction at next-to-leading order in chiral effective field theory. Nucl. Phys. A **954**, 273–293 (2016). https://doi.org/10.1016/j.nuclphysa.2016.01.006. arXiv:1511.05859

41. J. Haidenbauer, U.-G. Meißner, In-medium properties of a ΞN interaction derived from chiral effective field theory. Eur. Phys. J. A **55**(2), 23 (2019). https://doi.org/10.1140/epja/i2019-12689-2. arXiv:1810.04883

42. K. Miwa et al., Recent progress and future prospects of hyperon nucleon scattering experiment. EPJ Web Conf. **271**, 04001 (2022). https://doi.org/10.1051/epjconf/202227104001

43. S. Petschauer, N. Kaiser, J. Haidenbauer, U.-G. Meißner, W. Weise, Leading three-baryon forces from SU(3) chiral effective field theory. Phys. Rev. C **93**(1), 014001 (2016). https://doi.org/10.1103/PhysRevC.93.014001. arXiv:1511.02095

44. E. Epelbaum, W. Glöckle, U.-G. Meißner, The two-nucleon system at next-to-next-to-next-to-leading order. Nucl. Phys. A **747**, 362–424 (2005). https://doi.org/10.1016/j.nuclphysa.2004.09.107. arXiv:nucl-th/0405048

45. E. Epelbaum, H. Krebs, U.-G. Meißner, Improved chiral nucleon–nucleon potential up to next-to-next-to-next-to-leading order. Eur. Phys. J. A **51**(5), 53 (2015). https://doi.org/10.1140/epja/i2015-15053-8. arXiv:1412.0142

46. S. Petschauer, J. Haidenbauer, N. Kaiser, U.-G. Meißner, W. Weise, Hyperon-nuclear interactions from SU(3) chiral effective field theory. Front. Phys. **8**, 12 (2020). https://doi.org/10.3389/fphy.2020.00012. arXiv:2002.00424

47. J. J. de Swart, The Octet model and its Clebsch-Gordan coefficients. *Rev. Mod. Phys.*, 35:916–939, (1963) [Erratum: Rev. Mod. Phys. 37, 326–326 (1965)]. https://doi.org/10.1103/RevModPhys.35.916

48. J. Beringer et al., Review of particle physics (RPP). Phys. Rev. D **86**, 010001 (2012). https://doi.org/10.1103/PhysRevD.86.010001

49. E. Epelbaum, A. Nogga, W. Glöckle, H. Kamada, U.-G. Meißner, H. Witała, Few nucleon systems with two nucleon forces from chiral effective field theory. Eur. Phys. J. A **15**, 543–563 (2002). https://doi.org/10.1140/epja/i2002-10048-2. arXiv:nucl-th/0201064

50. S. Petschauer, N. Kaiser, Relativistic SU(3) chiral baryon–baryon Lagrangian up to order q^2. Nucl. Phys. A **916**, 1–29 (2013). https://doi.org/10.1016/j.nuclphysa.2013.07.010. arXiv:1305.3427

51. R.R. Scheerbaum, Spin-orbit splitting in nuclei near closed shells: (I). Contribution of the two-body spin-orbit interaction. Nucl. Phys. A **257**, 77–108 (1976). https://doi.org/10.1016/0375-9474(76)90476-0

52. J. Haidenbauer, U.-G. Meißner, A study of hyperons in nuclear matter based on chiral effective field theory. Nucl. Phys. A **936**, 29–44 (2015). https://doi.org/10.1016/j.nuclphysa.2015.01.005. arXiv:1411.3114

53. S. Petschauer, J. Haidenbauer, N. Kaiser, U.-G. Meißner, W. Weise, Hyperons in nuclear matter from SU(3) chiral effective field theory. Eur. Phys. J. A **52**(1), 15 (2016). https://doi.org/10.1140/epja/i2016-16015-4. arXiv:1507.08808

54. H. Akikawa et al., Hypernuclear fine structure in $^9_\Lambda$Be. Phys. Rev. Lett. **88**, 082501 (2002). https://doi.org/10.1103/PhysRevLett.88.082501

55. B. Sechi-Zorn, B. Kehoe, J. Twitty, R.A. Burnstein, Low-energy lambda-proton elastic scattering. Phys. Rev. **175**, 1735–1740 (1968). https://doi.org/10.1103/PhysRev.175.1735

56. G. Alexander, U. Karshon, A. Shapira, G. Yekutieli, R. Engelmann, H. Filthuth, W. Lughofer, Study of the Λ-n system in low-

energy Λ-p elastic scattering. Phys. Rev. **173**, 1452–1460 (1968). https://doi.org/10.1103/PhysRev.173.1452

57. R. Engelmann, H. Filthuth, V. Hepp, E. Kluge, Inelastic Σ-p interactions at low momenta. Phys. Lett. **21**(5), 587–589 (1966). https://doi.org/10.1016/0031-9163(66)91310-2

58. F. Eisele, H. Filthuth, W. Föhlisch, V. Hepp, G. Zech, Elastic $\Sigma^{\pm}$p scattering at low energies. Phys. Lett. B **37**, 204–206 (1971). https://doi.org/10.1016/0370-2693(71)90053-0

59. V. Hepp, H. Schleich, A new determination of the capture ratio $r_c = \frac{\sum^- p \to \sum^0 n}{(\sum^- p \to \sum^0 n) + (\sum^- p \to \Lambda^0 n)}$, the Λ^0 lifetime and the Σ^--Λ^0 mass difference. Z. Phys. **214**, 71 (1968). https://doi.org/10.1007/BF01380085

60. D. Stephen, PhD thesis, University of Massachusetts, (1970)

61. C.M. Vincent, S.C. Phatak, Accurate momentum-space method for scattering by nuclear and Coulomb potentials. Phys. Rev. C **10**, 391–394 (1974). https://doi.org/10.1103/PhysRevC.10.391

62. J. Haidenbauer, U.-G. Meißner, Status of the hyperon-nucleon interaction in chiral effective field theory. EPJ Web Conf. **271**, 05001 (2022). https://doi.org/10.1051/epjconf/202227105001. arXiv:2208.13542

63. J. Haidenbauer, U.-G. Meißner, S. Petschauer, Do $\Xi\Xi$ bound states exist? Eur. Phys. J. A **51**(2), 17 (2015). https://doi.org/10.1140/epja/i2015-15017-0. arXiv:1412.2991

64. J.K. Ahn et al., Σ^+p elastic scattering cross sections in the region of $350 \leq P_{\Sigma^+} \leq 750$MeV/c with a scintillating fiber active target. Nucl. Phys. A **761**, 41–66 (2005). https://doi.org/10.1016/j.nuclphysa.2005.07.004

65. R.A. Arndt, I.I. Strakovsky, R.L. Workman, An updated analysis of NN elastic scattering data to 1.6GeV. Phys. Rev. C **50**, 2731–2741 (1994). https://doi.org/10.1103/PhysRevC.50.2731. arXiv:nucl-th/9407035

66. SAID Partial-Wave Analysis. URL: https://gwdac.phys.gwu.edu/

67. Y. Kondo et al., Σ^-p elastic scattering in the region of 400 MeV/c $< P_{\Sigma^-} < 700$ Mev/c with a scintillating fiber active target. Nucl. Phys. A **676**, 371–387 (2000). https://doi.org/10.1016/S0375-9474(00)00191-3

68. L. Piekenbrock, (unpublished); cited and shown in Herndon et al. [69]

69. R.C. Herndon, Y.C. Tang, Phenomenological Λ-nucleon potentials from s-shell hypernuclei. 2. Dependence on intrinsic range. Phys. Rev. **159**, 853–861 (1967). https://doi.org/10.1103/PhysRev.159.853

70. J.A. Kadyk, G. Alexander, J.H. Chan, P. Gaposchkin, G.H. Trilling, Λp interactions in momentum range 300 to 1500 MeV/c. Nucl. Phys. B **27**, 13–22 (1971). https://doi.org/10.1016/0550-3213(71)90076-9

71. J.M. Hauptman, J.A. Kadyk, G.H. Trilling, Experimental study of Λp and Ξ^0p interactions in the range 1GeV/c-10GeV/c. Nucl. Phys. B **125**, 29–51 (1977). https://doi.org/10.1016/0550-3213(77)90222-X

72. M.M. Nagels, T.A. Rijken, J.J. De Swart, A potential model for hyperon–nucleon scattering. Ann. Phys. **79**, 338–385 (1973). https://doi.org/10.1016/0003-4916(73)90090-0

73. J. Nagata, H. Yoshino, V. Limkaisang, Y. Yoshino, M. Matsuda, T. Ueda, Phase-shift analysis of elastic Σ^+p scattering. Phys. Rev. C **66**, 061001 (2002). https://doi.org/10.1103/PhysRevC.66.061001

74. R. L. Workman et al. Review of Particle Physics. PTEP, 2022:083C01, (2022). https://doi.org/10.1093/ptep/ptac097

75. J. Haidenbauer, U.-G. Meißner, On the structure in the ΛN cross section at the ΣN threshold. Chin. Phys. C **45**(9), 094104 (2021). https://doi.org/10.1088/1674-1137/ac0e89. arXiv:2105.00836

76. J. Haidenbauer, U.-G. Meißner, The Jülich hyperon–nucleon model revisited. Phys. Rev. C **72**, 044005 (2005). https://doi.org/10.1103/PhysRevC.72.044005. arXiv:nucl-th/0506019

77. J. Haidenbauer, Coupled-channel effects in hadron–hadron correlation functions. Nucl. Phys. A **981**, 1–16 (2019). https://doi.org/10.1016/j.nuclphysa.2018.10.090. arXiv:1808.05049

78. Y. Kamiya, T. Hyodo, K. Morita, A. Ohnishi, W. Weise, $K^- p$ correlation function from high-energy nuclear collisions and chiral SU(3) dynamics. Phys. Rev. Lett. **124**(13), 132501 (2020). https://doi.org/10.1103/PhysRevLett.124.132501. arXiv:1911.01041

79. Y. Kamiya, K. Sasaki, T. Fukui, T. Hyodo, K. Morita, K. Ogata, A. Ohnishi, T. Hatsuda, Femtoscopic study of coupled-channels $N\Xi$ and $\Lambda\Lambda$ interactions. Phys. Rev. C **105**(1), 014915 (2022). https://doi.org/10.1103/PhysRevC.105.014915. arXiv:2108.09644

80. K. Miyagawa, W. Glöckle, Hypertriton calculation with meson theoretical nucleon–nucleon and hyperon nucleon interactions. Phys. Rev. C **48**, 2576 (1993). https://doi.org/10.1103/PhysRevC.48.2576

81. A. Nogga, H. Kamada, W. Glöckle, The Hypernuclei $^4_\Lambda$H and $^4_\Lambda$He: Challenges for modern hyperon nucleon forces. Phys. Rev. Lett. **88**, 172501 (2022). https://doi.org/10.1103/PhysRevLett.88.172501. arXiv:nucl-th/0112060

82. D. Gazda, T. Yadanar Htun, C. Forssén, Nuclear physics uncertainties in light hypernuclei. Phys. Rev. C **106**(5), 054001 (2022). https://doi.org/10.1103/PhysRevC.106.054001. arXiv:2208.02176

83. R. Wirth, R. Roth, Light neutron-rich hypernuclei from the importance-truncated no-core shell model. Phys. Lett. B **779**, 336–341 (2018). https://doi.org/10.1016/j.physletb.2018.02.021. arXiv:1710.04880

84. J. Haidenbauer, H. Le, U.-G. Meißner, A. Nogga, in preparation

85. M. Juric et al., A new determination of the binding-energy values of the light hypernuclei ($15 \geq A$). Nucl. Phys. B **52**, 1–30 (1973). https://doi.org/10.1016/0550-3213(73)90084-9

86. P. Eckert et al., Commissioning of the hypertriton binding energy measurement at MAMI. EPJ Web Conf. **271**, 01006 (2022). https://doi.org/10.1051/epjconf/202227101006

87. T. Gogami et al., High accuracy spectroscopy of 3- and 4-body Λ hypernuclei at Jefferson Lab. EPJ Web Conf. **271**, 01001 (2022). https://doi.org/10.1051/epjconf/202227101001

88. P. Maris et al., Nuclear properties with semilocal momentum-space regularized chiral interactions beyond N2LO. Phys. Rev. C **106**(6), 064002 (2022). https://doi.org/10.1103/PhysRevC.106.064002. arXiv:2206.13303

89. J. Haidenbauer, U.-G. Meißner, A. Nogga, Constraints on the Λ-neutron interaction from charge symmetry breaking in the $^4_\Lambda He$ - $^4_\Lambda H$ hypernuclei. Few Body Syst. **62**(4), 105 (2021). https://doi.org/10.1007/s00601-021-01684-3. arXiv:2107.01134

90. D. Gazda, A. Gal, Charge symmetry breaking in the A = 4 hypernuclei. Nucl. Phys. A **954**, 161–175 (2016). https://doi.org/10.1016/j.nuclphysa.2016.05.015. arXiv:1604.03434

91. P. Eckert, P. Achenbach, et al. URL: https://hypernuclei.kph.uni-mainz.de/

92. A. Gal, E.V. Hungerford, D.J. Millener, Strangeness in nuclear physics. Rev. Mod. Phys. **88**(3), 035004 (2016). https://doi.org/10.1103/RevModPhys.88.035004. arXiv:1605.00557

93. J. Haidenbauer, U.-G. Meißner, N. Kaiser, W. Weise, Lambda-nuclear interactions and hyperon puzzle in neutron stars. Eur. Phys. J. A **53**(6), 121 (2017). https://doi.org/10.1140/epja/i2017-12316-4. arXiv:1612.03758

94. D. Gerstung, N. Kaiser, W. Weise, Hyperon-nucleon three-body forces and strangeness in neutron stars. Eur. Phys. J. A **56**(6), 175 (2020). https://doi.org/10.1140/epja/s10050-020-00180-2. arXiv:2001.10563

95. Y. Fujiwara, Y. Suzuki, C. Nakamoto, Baryon–baryon interactions in the SU(6) quark model and their applications to light nuclear systems. Prog. Part. Nucl. Phys. **58**, 439–520 (2007). https://doi.org/10.1016/j.ppnp.2006.08.001. arXiv:nucl-th/0607013

96. T. Inoue, Strange Nuclear Physics from QCD on Lattice. AIP Conf. Proc. **2130**(1), 020002 (2019). https://doi.org/10.1063/1.5118370. arXiv:1809.08932

97. E. Friedman, A. Gal, Constraints on $\Xi-$ nuclear interactions from capture events in emulsion. Phys. Lett. B **820**, 136555 (2021). https://doi.org/10.1016/j.physletb.2021.136555. arXiv:2104.00421

98. S. Binder et al., Few-nucleon systems with state-of-the-art chiral nucleon–nucleon forces. Phys. Rev. C **93**(4), 044002 (2016). https://doi.org/10.1103/PhysRevC.93.044002. arXiv:1505.07218

99. R.J. Furnstahl, N. Klco, D.R. Phillips, S. Wesolowski, Quantifying truncation errors in effective field theory. Phys. Rev. C **92**(2), 024005 (2015). https://doi.org/10.1103/PhysRevC.92.024005. arXiv:1506.01343

100. P. Achenbach, Charge Symmetry Breaking in Light Hypernuclei. Few Body Syst. **58**(1), 17 (2017). https://doi.org/10.1007/s00601-016-1178-x

101. Stefan Petschauer. private communication

102. M. Frink, U.-G. Meißner, On the chiral effective meson-baryon Lagrangian at third order. Eur. Phys. J. A **29**, 255–260 (2006). https://doi.org/10.1140/epja/i2006-10105-x. arXiv:hep-ph/0609256

103. J.A. Oller, M. Verbeni, J. Prades, Meson-baryon effective chiral Lagrangians to $\mathcal{O}(q^3)$. JHEP **09**, 079 (2006). https://doi.org/10.1088/1126-6708/2006/09/079. arXiv:hep-ph/0608204

104. M. Frink, U.-G. Meißner, Chiral extrapolations of baryon masses for unquenched three flavor lattice simulations. JHEP **07**, 028 (2004). https://doi.org/10.1088/1126-6708/2004/07/028. arXiv:hep-lat/0404018

105. M. Hoferichter, J. Ruiz de Elvira, B. Kubis, U.-G. Meißner, Matching pion-nucleon Roy-Steiner equations to chiral perturbation theory. *Phys. Rev. Lett.*, 115(19):192301, (2015) https://doi.org/10.1103/PhysRevLett.115.192301. arXiv:1507.07552

106. M. Hoferichter, J. Ruiz de Elvira, B. Kubis, U.-G. Meißner, Roy–Steiner-equation analysis of pion–nucleon scattering. *Phys. Rept.*, 625:1–88, https://doi.org/10.1016/j.physrep.2016.02.002. arXiv:1510.06039 (2016)

107. S. Petschauer, J. Haidenbauer, N. Kaiser, U.-G. Meißner, W. Weise, Density-dependent effective baryon-baryon interaction from chiral three-baryon forces. Nucl. Phys. A **957**, 347–378 (2017). https://doi.org/10.1016/j.nuclphysa.2016.09.010. arXiv:1607.04307

108. V. Bernard, N. Kaiser, U.-G. Meißner, Chiral dynamics in nucleons and nuclei. Int. J. Mod. Phys. E **4**, 193–346 (1955). https://doi.org/10.1142/S0218301395000092. arXiv:hep-ph/9501384